

Exceptional stability of a perilipin on lipid droplets depends on its polar residues, suggesting multimeric assembly

Manuel Giménez-Andrés^{1,2}, Tadej Emeršič³, Sandra Antoine-Bally¹, Juan Martín D'Ambrosio^{1,7}, Bruno Antonny⁴, Jure Derganc^{3,5}, Alenka Čopić^{1,6,7}

1. Institut Jacques Monod, CNRS, UMR 7592, Université de Paris, France
2. Université Paris-Saclay, 91190, Saint-Aubin, France
3. Institute of Biophysics, Faculty of Medicine, University of Ljubljana, Slovenia
4. Université Côte d'Azur, CNRS, IPMC, UMR7275, 06560 Valbonne, France
5. Chair of Microprocess Engineering and Technology – COMPETE, University of Ljubljana, Slovenia
6. Corresponding author: alenka.copic@crbm.cnrs.fr
7. Current address: CRBM, CNRS, UMR 5237, Université de Montpellier, 1919 route de Mende, 34293 Montpellier, France

Impact Statement: The amphipathic helix of perilipin 4 relies on the organization of its polar residues to form a remarkably immobile and stable protein layer on the surface of lipid droplets.

Keywords: lipid droplet, perilipin 4, amphipathic helix, adipocyte, apolipoprotein, lipid droplet size

Abstract

Numerous proteins target lipid droplets (LDs) through amphipathic helices (AHs). It is generally assumed that AHs insert bulky hydrophobic residues in packing defects at the LD surface. However, this model does not explain the targeting of perilipins, the most abundant and specific amphipathic proteins of LDs, which are weakly hydrophobic. A striking example is Plin4, whose gigantic and repetitive AH lacks bulky hydrophobic residues. Using a range of complementary approaches, we show that Plin4 forms a remarkably immobile and stable protein layer at the surface of cellular or in vitro generated oil droplets, and decreases LD size. Plin4 AH stability on LDs is exquisitely sensitive to the nature and distribution of its polar residues. These results suggest that Plin4 forms stable arrangements of adjacent AHs via polar/electrostatic interactions, reminiscent of the organization of apolipoproteins in lipoprotein particles, thus pointing to a general mechanism of AH stabilization via lateral interactions.

Introduction

Lipid droplets (LDs) are cellular organelles specialized for storage of lipids and maintenance of cellular lipid homeostasis. They are composed of a neutral lipid core that is covered by a monolayer of phospholipids and other amphiphilic lipids, and by proteins (Thiam et al., 2013b; Olzmann and Carvalho, 2019). LDs vary in size over four orders of magnitude, depending on organism/cell type and fasting state of a cell; in mature adipocytes, the majority of the cell can be occupied by a single LD measuring $>100\ \mu\text{m}$ in diameter (Lundquist et al., 2020; Stenkula and Erlanson-Albertsson, 2018). Secreted lipoprotein particles are similar to LDs in terms of their over-all composition but are much smaller, ranging from 10 to 1000 nm in diameter (Ohsaki et al., 2014).

Different types of proteins have been found to associate with LDs (Brasaemle et al., 2004; Bersuker et al., 2018; Kory et al., 2015; Pataki et al., 2018; Mejhert et al., 2020). They can be either stably embedded in the LD monolayer, coming by diffusion from the endoplasmic reticulum (ER), from which LDs emerge, or they associate with LDs peripherally from the cytosol (Ohsaki et al., 2014; Bersuker and Olzmann, 2017). Many of them are enzymes involved in lipid synthesis or hydrolysis, for example triglyceride synthases, acyltransferases, lipases and their inhibitors or activators (Wilfling et al., 2013; Zechner et al., 2017). Proteins can also regulate LDs in a non-enzymatic manner. A prominent example is the perilipins: in mammals, this is a family of five proteins that share related structural features and are highly abundant on LDs (Sztalryd and Brasaemle, 2017). They vary in their tissue distribution: Plin2 and Plin3 are widely expressed, whereas Plin1 and Plin4 are most highly expressed in adipocytes, and Plin5 is enriched in oxidative tissues (Wolins et al., 2006; Brasaemle et al., 2004; Wolins et al., 2003). Plin4 and Plin5 are also enriched in muscle tissues. Less closely related abundant LD proteins have been identified in many other species (Gao et al., 2017; Granneman et al., 2017; Miura et al., 2002). Whereas perilipins contain no known enzymatic motifs, a number of them, in particular Plin1, have been shown to regulate the recruitment of lipases to the LD surface (Sztalryd and Brasaemle, 2017).

Many LD-localized proteins use amphipathic helices (AHs) to directly interact with the LD lipid surface (Bersuker and Olzmann, 2017; Giménez-Andrés et al., 2018). All mammalian perilipins contain a predicted AH region in their N-terminal part, which has been shown to be important for their LD localization (McManaman et al., 2003; Nakamura and Fujimoto, 2003;

Bulankina et al., 2009; Rowe et al., 2016; Copic et al., 2018). This region is composed of 11-aa repeats that would fold into a 3-11 helix, a slightly extended variant of an α -helix that was characterized in α -synuclein and in apolipoproteins (Bussell and Eliezer, 2003; Jao et al., 2008). Other regions, including a C-terminal region that can fold into a 4-helix bundle (Hickenbottom et al., 2004), can also contribute to LD targeting to varying extents (Targett-Adams et al., 2003; Subramanian et al., 2004; Nakamura et al., 2004; Ajjaji et al., 2019). Interestingly, both the 11-aa repeat region and the 4-helix bundle bear structural similarities with apolipoproteins, which are required for formation of lipoprotein particles (Saito et al., 2003; Melchior et al., 2017).

The 11-aa repeat AH region is by far the longest in Plin4, containing close to 1000 aa in the human protein, with repeats that are highly homologous at the 33-aa level (Copic et al., 2018; Scherer et al., 1998). The aa composition of Plin4 AH reveals a striking bias towards small hydrophobic residues, in particular V, T and A, whereas large residues such as W and F are almost entirely absent (Figure 1A). We have demonstrated that the Plin4 AH region is unfolded in solution, but adopts a highly helical structure in contact with a lipid surface. The low hydrophobicity of this AH promotes specific targeting to LDs, which are permissive for the binding of many amphipathic proteins (Copic et al., 2018; Prévost et al., 2018). This is likely due to the physical properties of the LD surface, where the spreading of the phospholipid monolayer leads to exposure of the hydrophobic core with which the hydrophobic face of an AH can interact more strongly (Bacle et al., 2017; Chorlay et al., 2019). Due to its extreme length, Plin4 in particular can cover a large LD surface and could act as a substitute for phospholipids (Copic et al., 2018). A recent study has identified expansion of Plin4 33-aa repeats in a family with a rare autosomal dominant progressive myopathy, underscoring the importance of studying this protein (Ruggieri et al., 2020).

Due to their high abundance on LDs, perilipins are often referred to as LD coat proteins (Sztalryd and Brasaemle, 2017). Protein coats have been well characterized on transport vesicles, for example COPI, COPII and clathrin coat. In all these cases, the coat forms in a tightly controlled manner by sequential recruitment of coat subunits on the membrane surface (Schekman and Orci, 1996; Taylor et al., 2011). Importantly, coat subunits laterally interact to form a highly polymerized structure covering the surface of a vesicle (Faini et al., 2013). Coat polymerization is in fact the main force that generates these membrane vesicles (Saleem et al., 2015). Perilipins have not been shown to be directly involved in LD budding from the ER;

LD formation may be principally driven by lipids, with proteins playing a more regulatory role (Ben M'barek et al., 2017; Chorlay et al., 2019; Santinho et al., 2020). On the other hand, COPI coat components have also been observed to bind to and influence LDs and to regulate recruitment of other LD proteins (Guo et al., 2008; Thiam et al., 2013a; Wilfling et al., 2014; Soni et al., 2009).

Here, we ask whether perilipins possess any of the qualities traditionally associated with protein coats. We focus on the 11-aa repeat AH regions of mammalian perilipins, which directly associate with the lipid surface of LDs. We analyze the stability of perilipin AHs on the lipid surface and their ability to form an immobile structure using various cellular and biochemical approaches, as well as a novel microfluidics set-up to follow the interaction of AHs with oil over time. We show that one perilipin, Plin4, is capable of making highly stable protein-lipid structures by forming an immobile coat on the surface of pure oil or LDs in cells using its unique AH. The Plin4-oil droplets remain stable over the course of many days. In contrast, the interaction of the AHs from other perilipins with LDs or with oil is highly dynamic. The stability of interaction correlates with the size of oil particles, which are smaller in the case of Plin4. Extensive mutagenesis shows that the AH of Plin4 can form an immobile coat due to its organized structure that could enable interhelical interactions on the lipid surface. This model is supported by our measurement of Plin4 density, which reveals tight packing of helices on oil surface.

Results

Purified Plin4 AH forms very stable protein-oil emulsions

We have previously shown that the AH of Plin4 is optimized for LD binding both by its length and particular aa composition (Copic et al., 2018). The AH sequence of human Plin4 is composed of ~29 highly homologous 33-aa repeats (Figure 1A). The efficiency of LD targeting correlated with AH length: at least four 33-aa repeats of the wild-type Plin4 AH were needed to detect some LD localization in HeLa cells (Figure 1B). Furthermore, the strong bias towards small residues is decisive for LD targeting: mutations that increased hydrophobicity (T > V) made Plin4 promiscuous for other organelles besides LDs; mutations that decreased hydrophobicity (T > S) rendered Plin4 cytosolic (Figure 1B).

The amphipathic region of Plin4 is capable of emulsifying triolein upon vigorous mechanical mixing (vortex) in aqueous buffer in the absence of any other surfactant, such as phospholipids. A similar result was obtained with a shorter Plin4 AH construct containing 4 33-aa repeats (Plin4 4mer) or a longer construct comprising 12 33-aa repeats (Plin4 12mer) (Figure 1C) (Copic et al., 2018). Electron microscopy and dynamic light scattering (DLS) revealed that emulsions of triolein and Plin4 12mer contained spherical oil particles with a large range of sizes; typically with a diameter of 50 to 500 nm (mean \approx 200 nm), although some larger particles (diameter > 1 μ m) could also be observed (Copic et al., 2018). We focused on these latter particles, whose size made them suitable for imaging by fluorescence light microscopy. For this, we performed triolein emulsification in the presence Plin4 12mer or Plin4 4mer labelled with the fluorescent dye Alexa488 (Plin4 12mer-A488), mixed with unlabelled Plin4 AH of the same length. The spherical particles displayed a homogenous fluorescent surface, which allowed us to perform dynamics measurements by fluorescence recovery after photobleaching (FRAP) (Figure 1D, E).

In the first FRAP protocol, we bleached an entire Plin4-oil particle. In this case, fluorescence recovery should occur by exchange between free Plin4 AH-A488 in solution and bleached Plin4 AH-A488 molecules bound to the lipoparticle surface. As shown in Figure 1D, E, we detected no recovery within the time range of the measurement (3 min). In the second FRAP protocol, we bleached a limited area of the lipoparticle surface to follow fluorescence recovery of Plin4 AH molecules by lateral diffusion. Again, we observed no recovery within

5 minutes after bleaching, neither with Plin4 4mer nor Plin4 12mer (Figure 1D, E). Thus, Plin4 AH forms a very stable and immobile coat at the surface of triolein.

To gain further insight into the stability of the Plin4 AH/triolein particles, we visualized the emulsions prepared with fluorescent Plin4 12mer over 7 days after the vortexing step. As shown in Figure 1F, the emulsions at $t = 15$ min, 75 min, 4 days and 7 days appeared very similar, showing numerous submicrometer particles and a few larger ($> 1 \mu\text{m}$) particles. Importantly, most if not all particles remained isolated during this long observation time, showing no obvious clustering or aggregation.

For comparison, we used a mutated form of Plin4 4mer (4T>S), in which several threonines in the hydrophobic face of the amphipathic region had been replaced by the more polar residue serine (Figure 1A). Plin4(4T>S) was purified from bacteria following the same procedure as for Plin4 4mer or Plin4 12mer. This mutant was inefficient at emulsifying olein (Figure 1C), in agreement with its inability to target LDs in HeLa cells (Figure 1B) (Copic et al., 2018). However, we could observe a few large triolein droplets formed by fluorescently-labelled Plin4(4T>S). The lipoparticles covered by Plin4(4T>S) clustered over time, suggesting that their coat was much less protective than that observed with Plin4 12mer (Figure 1F). FRAP analysis of these particles revealed a variable behavior of Plin4(4T>S), in agreement with its decreased emulsifying capacity and the tendency to cluster; some clustering could already be detected in some of the FRAP recovery time-courses (Figure 1 – figure supplement 1).

Analysis by DLS revealed an even more remarkable stability of Plin4 12mer-oil particles over time, as we detected no change in particle size distribution even 28 days after emulsification (Figure 1G). This puts Plin4 AH on par with natural emulsifiers used for technological purposes in food or pharmaceutical industry (McClements and Gumus, 2016). In contrast, the particles formed by Plin4(4T>S) were too heterogenous for analysis by DLS even at the first time-point (3h) after emulsion formation.

Following Plin4-oil interaction in real time using microfluidics

To further study the interaction of Plin4 AH with neutral lipids, we required a method where we could present the AH to the oil surface in a gentle manner and follow in real time the assembly of protein on the oil surface. We developed a microfluidics system, in which we

used a glass chip with two channels joined by a T-junction. We introduced the water-based buffer into the main channel and pure triolein into the side channel and stabilized the buffer-triolein interface 50-100 μm below the T-junction by closing the valve in the side-channel (Figure 2A). In this configuration, the buffer-triolein interface is not disturbed by the flow in the main channel, whereas the solutes from the main channel are free to diffuse to the oil surface. In terms of diffusion and hydrodynamic characteristics, this system is similar to microfluidic cavities (Osterman et al., 2016; Vrhovec et al., 2011).

We introduced Alexa-488-labelled Plin4 12mer into the main channel, and we followed the change in fluorescent signal inside the side channel and on the triolein interface over time using a confocal microscope (Figure 2B and Videos 1-4). As the protein solution in the main channel reached the T-junction we could observe its diffusion into the side channel (Video 1). After several seconds, we detected an increase in fluorescence on the oil interface, which stabilized in ≈ 3 min at a level 3-fold higher than the fluorescence of the solution (Figure 2C). We then replaced the protein solution in the main channel with buffer to promote protein dissociation (Video 2). However, the fluorescence at the interface remained constant, indicating a stable interaction between Plin4 12mer and oil. No enrichment of fluorescence on the oil interface was observed when we introduced buffer containing Alexa488 conjugated to free cysteine instead of Plin4 12mer (lower row in Figure 2B,C and Videos 3,4). These experiments confirm that Plin4 AH forms a very stable protein layer at the oil/water interface. Fluorescent protein also adsorbed to the glass surface and intercalated into the glass-oil interface. The chemically heterogeneous glass surface induced a marked hysteresis in oil-glass contact angle (Joanny and De Gennes, 1984) (Figure 2 – figure supplement 1), which allowed us to apply the Laplace law and verify that the protein adsorption lowered the surface tension of the oil interface (Figure 2 – figure supplement 1).

We compared the interaction Plin4 12mer with oil to that of the less hydrophobic Plin4(4T>S) mutant using the microfluidics system. The mutant assembled on the oil surface with no measurable difference in the kinetics of assembly or in the factor of enrichment compared to Plin4 12mer. The difference between Plin4 12mer and Plin4(4T>S) became obvious when the two proteins were used as unlabelled proteins at a 50:1 molar excess over labelled Plin4 12mer. We observed strong fluorescent signal on the oil interface in the presence of the Plin4(4T>S) mutant, but not in the presence of Plin4 12mer, indicating that the wild-type protein out-competed with Plin4(4T>S) for oil coating (Figure 2—figure supplement 2).

Comparison between the AH of Plin4 and other perilipins

So far, we focused on the interaction between the AH of Plin4 and LDs as it represents a most striking example of an LD-binding AH. We wanted to specifically compare the characteristics and LD-binding properties of Plin4 AH with the AH regions of the other human perilipins (Plin1, Plin2, Plin3), which have been shown to contribute to their LD targeting (McManaman et al., 2003; Nakamura and Fujimoto, 2003; Bulankina et al., 2009; Rowe et al., 2016). The number of 11-aa repeats that we could identify in each Plin protein ranged from 5 for Plin5 to about 8 for Plin1/2/3, compared to the 87 repeats in Plin4. In addition, the repeats are more highly conserved in Plin4, and Plin4 AH is also striking for the absence of any deletions or insertions between the repeats (Copic et al., 2018) (Figure 3A). Comparison of the composition of the 11-aa regions showed that they were similar in character in Plin2/3/4, with low hydrophobicity due to a lack of large hydrophobic residues (Figure 3B). Plin1 AH is somewhat more hydrophobic and contains some aromatic residues. A more divergent character of this AH is consistent with the evolutionary divergence of Plin1 from the other perilipins (Granneman et al., 2017). The AH of Plin5 is shorter than in other perilipins and we did not consider it in further analysis.

We first expressed Plin AHs as GFP fusions in budding yeast and assessed their ability to target LDs. Budding yeast was used previously for expression of mammalian perilipins; full-length Plin1, Plin2 and Plin3, as well as their N-terminal halves, which include a region termed 'PAT domain' in addition to 11-aa repeats, targeted LDs in this system (Jacquier et al., 2013; Rowe et al., 2016; Copic et al., 2018). We expressed the AHs of Plin1, Plin2, and Plin3, and fragments of different lengths from the AH region of Plin4, containing 4, 6, or 12 33-aa repeats (132, 198 and 396 aa, respectively). In the case of Plin3, we could not observe any expression of just the AH region (aa 113-205) fused to GFP, therefore we added some additional upstream sequence (aa87-205) (Bulankina et al., 2009). We expressed these constructs under three growth conditions that promote LD accumulation in yeast (Gao et al., 2017) : (i) wild-type cells grown to stationary phase; (ii) stationary phase cells lacking the most abundant yeast LD protein, Pet10p/Plin1p (*pet10Δ*); (iii) *pet10Δ* cells grown in oleic-acid rich medium, which promoted the formation of large LDs (*pet10Δ* + OA). In wild-type cells, Plin1 AH, but not Plin2 AH, Plin3 AH or Plin4 4mer, could be observed on LDs (Figure 3C). In contrast to Plin4 4mer, Plin4 6mer and Plin4 12mer localized to LDs, in line with our

finding that increasing the AH length improves LD targeting (Copic et al., 2018). In agreement with the work of Gao et al., deletion of Pet10p/Plin1p improved LD targeting of our mammalian constructs, presumably because more LD surface was available (Kory et al., 2015). Targeting to LDs was further increased by the addition of oleic acid to stationary phase cells, which induced large LDs (Figure 3C). In addition, we observed some protein at the PM, in particular in the case of Plin4 AH, consistent with observations from human cells and tissues (Scherer et al., 1998; Ruggieri et al., 2020). Based on these results, we conclude that the 11-aa repeat regions of Plin1, Plin2, Plin3, and Plin4 are all sufficient for targeting LDs. Comparison of different growth conditions (Figure 3D), and the fact that all Plin AHs were expressed at similar levels (Figure 3—figure supplement 1B), allowed us to establish a ranking of Plin AH-LD affinities. Extrapolating to its full length, Plin4 AH has the highest affinity for LDs, followed by Plin1 AH, and finally by Plin2 AH and Plin3 AH. However, correcting for length differences reveals that per unit of AH length, Plin1 AH has a higher affinity for LDs than AHs of Plin2, Plin3 or Plin4. This is consistent with the higher hydrophobicity of Plin1 AH compared to other perilipin AHs (Figure 3B); higher hydrophobicity has been shown to promote LD binding (Copic et al., 2018; Prévost et al., 2018).

Strikingly, we noticed a difference in the size of the LDs that formed in *pet10Δ* cells grown in oleic acid-rich medium, depending on the AH expressed (Figure 3C,E): LDs were significantly larger (2.5-fold difference in projected area, which would correspond to a 4-fold difference in volume) when covered with Plin1, Plin2 or Plin3 AH, compared to LDs covered with Plin4 12mer (Figure 3C,E). LDs with Plin4 6mer were also somewhat larger than those covered with Plin4 12mer. LDs with Plin4 4mer were more variable in size and appearance, preventing the use of the same quantification protocol.

We conclude that AHs from all four perilipins (Plin1-4) can target LDs and that their affinity for LDs correlates with their length and hydrophobicity. However, the AH of Plin4 could reduce the size of LDs more strongly than the AHs of other perilipins.

Stability of binding of perilipin AHs to LDs in model cellular systems

We used FRAP to assess the stability of AH binding to yeast LDs. Plin2 AH-GFP and Plin3 AH-GFP could readily exchange between LD surface and the cytosol in cells grown for 24h

in oleic acid medium, as reflected by a recovery half-life on the order of a few seconds (Figure 4A). The exchange of Plin1 AH-GFP was 2-3 times slower, consistent with results obtained in mammalian cells with N-terminal halves of Plin1, Plin2 and Plin3 (Ajjaji et al., 2019). In striking contrast, Plin4 12mer-GFP displayed almost no recovery on LDs over a period of more than 5 min (Figure 4A). We observed a similar difference between Plin1 AH and Plin4 12mer in cells grown for to early stationary phase in standard growth medium (Figure 4B). However, these LDs were much smaller and more mobile, leading to a large variability in the fluorescence measurement. Due to small size of these LDs, we could not perform a partial FRAP to assess the lateral mobility of Plin AH constructs on LD surface as we did for Plin4 AH on oil in vitro. However, we took advantage of the fact that both Plin4 AH and Plin1 AH also localized to the yeast PM in *pet10Δ* cells (Figure 4C). Bleaching a small area on the PM in exponentially growing cells showed that Plin4 12mer was highly immobile. Mobility of Plin4 AH at the PM was increased when we used shorter constructs (8mer and 6mer), in agreement with the correlation between AH length and binding affinity (Figure 4D and Copic et al., 2018). However, even for the shortest Plin4 AH construct for which we consistently observed targeting to yeast membranes, the recovery after photobleaching was at least an order of magnitude slower than for Plin1 AH or Plin3 AH. Given that all AH constructs were expressed at similar levels (Figure 3 – figure supplement 1), i.e., the differences in the kinetics were not due to differences in protein concentration, we conclude that, in addition to its length, the particular composition of the Plin4 AH enables its stable binding to LDs.

We also tested the dynamics of Plin4 12mer-LD interaction in *Drosophila* Schneider 2 (S2) cells (Figure 4 – figure supplement 1A). These cells were used to decipher mechanisms of LD homeostasis (Guo et al., 2008; Krahmer et al., 2011), and we previously demonstrated that expression of Plin4 12mer in S2 cells rescued the increase in size of LDs following the depletion of phosphatidylcholine (PC) (Copic et al., 2018). Interestingly, we observed a large cell-to-cell variability in the FRAP recovery curves of Plin4 12mer-GFP on LDs; whereas in some cells Plin4-12mer on LDs was largely immobile (half-time of recovery >100s), similar to our results in yeast, in other cells the recovery could be on the order of 1 s (Figure 4 – figure supplement 1A; note that within the same cell, the signal on all LDs recovered at the same rate). PC depletion upon CCT α knocked-down had a small effect, but this was not the main driver of cell-to-cell variability (Figure 4 - Supplement 1B). The level of protein expression was also not very predictive of recovery rate. In contrast, we observed a

correlation between the rate of FRAP recovery and the intensity of the Plin4 fluorescent signal on LDs (Figure 4 - Supplement 1C). This observation suggests that Plin4 AH density at the LD surface influences its dynamics, a feature reminiscent of protein coats. At low membrane coverage level, coat subunits diffuse and exchange quickly; at high membrane coverage level, their polymerization by side-side interaction prevents lateral mobility and fast turnover (Saleem et al., 2015; Sorre et al., 2012).

Comparison of proteolipid droplets formed with Plin4 AH or Plin3 AH

To study in more detail the difference between Plin4 and other perilipin AHs binding to LDs, we used our *in vitro* assays to compare the behavior of purified Plin4 AH fragments with that of Plin3 AH. We chose Plin3 AH because it displayed a similar steady-state distribution in yeast as the slightly longer Plin4 4mer, however, it showed a rapid exchange between LDs and the cytosol and it did not decrease LD size in oleic acid media. Mixing purified Plin3 AH with oil resulted in a highly turbid suspension, similar to the suspensions obtained with Plin4 4mer or Plin4 12mer (Figure 5A and Figure 5 – figure supplement 1). By DLS, Plin4 4mer-oil droplets behaved like Plin4 12mer oil droplets (see Figure 1G), displaying a particle size profile with a single peak that did not change over 14 days (Figure 5B, left panel). In contrast, the droplets produced by Plin3 AH were more heterogenous with larger peak sizes already 3h after droplet formation. Thereafter, we observed a spreading of the peaks until the samples became too complex for DLS analysis (14 days after formation Figure 5B, right panel). Such complexity is generally due to the presence of particles of variable sizes, suggesting that Plin3 AH-oil particles were undergoing fusion due to less stable coating by Plin3 AH. We verified using circular dichroism (CD) that this difference was not due to poor folding of the Plin3 helix (Figure 5 – figure supplement 1B): folding of Plin3 AH in the presence of the helix-inducing reagent trifluoroethanol (TFE) was similar to what we previously showed for Plin4 AH (Copic et al., 2018; see also Figure 6 – figure supplement 1).

Centrifugation of AH-oil suspensions on sucrose gradients revealed a smaller fraction of total Plin3 AH protein associated with the oil fraction (top of the gradients) than Plin4 4mer or Plin4 12mer (Figure 5C,D). This could be either because less Plin3 AH was bound to the oil droplets or because Plin3 AH bound to oil less strongly and dissociated during centrifugation. To distinguish between these possibilities, we performed competition experiments in which we first formed protein-oil droplets by mixing oil with a high concentration of unlabelled purified AH constructs (Plin4 12mer, Plin4 4mer or Plin3 AH). Then, we gently added

Alexa488-labelled Plin4 12mer at an excess mass ratio of 20:1 compared to unlabelled protein, and we monitored the fluorescence of the suspensions over time using confocal microscopy (Figure 5E). Consistent with our previous results, we observed no incorporation of fluorescent Plin4 12mer into the preformed Plin4 12mer-oil particles over a period of 24 h, unless we vortexed the suspension (Figure 5E,F; top panel). We could observe some incorporation of fluorescent Plin4 12mer into Plin4 4mer-oil particles after 3 or 24 hours of incubation, in agreement with a more stable binding of a 3-times longer AH and our cellular data (Figure 5E,F; middle panel). In striking contrast, when we pre-formed AH-oil particles using Plin3 AH, Plin4 12mer readily incorporated into these particles, reaching close to maximal particle fluorescence within 10 min after Plin4 12mer addition (Figure 5E,F; bottom panel). In agreement with the DLS data, we also observed clustering of Plin3 AH-formed oil particles, especially after 24 hours of incubation. Because Plin3 AH is only 1.5-times shorter than Plin4 4mer, yet it displays a significantly less stable binding to oil droplets in vitro and to LDs in cells, we conclude that the specific sequence of Plin4 AH is predominantly responsible for its highly stable interaction with LDs.

The nature and distribution of aa in the polar face of Plin4 AH is critical for LD targeting

The Plin4 AH sequence displays a remarkable repetitiveness (Figure 3A). Positions of polar and charged residues are extremely conserved among the 33-aa repeats (Figure 6A). Furthermore, the sequence shows a strong preference for lysine over arginine (22-fold) and for aspartic over glutamic acid (18-fold) (Figure 3B). These considerations prompted us to construct mutants of Plin4 4mer in which we introduced in every 33-aa repeat modest mutations (e.g. N>Q, D>E, or K>R) that should not modify the folding and overall physical chemistry of the helix, including its charge and hydrophobic moment.

We first focused on the two conserved amide residues: an asparagine present in 25 out of 29 repeats of human Plin4, and a glutamine seven residues apart and conserved in all repeats (Figure 6A). The N[x]₆Q sequence was replaced by N[x]₆N (NN), Q[x]₆Q (QQ) or Q[x]₆N (QN). Strikingly, these three mutations almost eliminated the targeting of Plin4 4mer to LDs in HeLa cells (Figure 6C). We purified the NN 4mer mutant to verify by CD that this mutation did not prevent helical folding. Like Plin4 4mer and Plin4(4T>S), this mutant was unfolded in solution but displayed a strong helical signal in the presence of TFE (Figure 6 – figure supplement 1). Next, we considered the charged residues. Replacing all aspartates with glutamates (2D>E) led to a small decrease in AH targeting to LDs in HeLa cells, whereas

replacing the lysine residues with arginine (3K>R) almost abolished AH targeting to LDs (Figure 6B,C). These results suggested that a precise interaction between charged and/or polar residues could be important for LD binding.

We also noted an unusual distribution of charged residues throughout the Plin4 AH sequence, with positive ones always lying on one side of the helix close to the apolar/polar interface (Figure 6D). To test whether charged residues in Plin4 AH could mediate interhelical interaction at the LD surface, we prepared a mutant of Plin4 12mer in which we reorganized the distribution of charges in the polar face of all 33-mer repeats without changing the overall composition (Figure 6D). This more symmetric Plin4 12mer AH mutant, termed charge-swap (csw), was similar to a 4mer mutant that we tested previously and which did not localize to LDs when expressed in HeLa cells (Copic et al., 2018). We observed some localization of the longer csw 12mer-GFP mutant to LDs in HeLa cells, which was significantly reduced compared to Plin4 12mer-GFP (Figure 6E). We verified by CD spectroscopy using purified csw 12mer that the permutations of the sequence did not affect its helical folding (Figure 6F and Figure 6 – figure supplement 2A). When we compared the localization of these two constructs in the yeast model, we observed a difference in their distribution between LDs and the PM, with csw 12mer showing a lower ratio of LD-to-PM signal compared to Plin4 12mer (Figure 6G and Figure 6 – figure supplement 2B). This preference for the PM is consistent with the distribution of positive charges in the csw 12mer helix, which is optimal for mediating electrostatic interactions with the negative surface of the PM. We also noted a small shift towards a larger size LDs surrounded by csw 12mer, compared to Plin4 12mer (Figure 6 – figure supplement 2C).

A previous analysis of the binding properties of disparate AHs to LD suggested the importance of large hydrophobic residues for LD binding (Prévoist et al., 2018). Although the aa composition of perilipin AHs does not fit with this model, we tested whether increasing the hydrophobicity of Plin4 AH could by itself be sufficient for a highly stable LD binding, without the contribution of the polar face. For this, we compared the dynamic behavior of two previously characterized Plin4 4mer mutants in HeLa cells, a more hydrophobic 2T>V (containing in total 8 substitutions in the four repeats), and 2T>V csw, which in addition has a reorganized polar face (Copic et al., 2018). Strikingly, whereas 2T>V exhibited slow recovery curves by FRAP in HeLa cells, the recovery was ~60 times faster for the 2T>V csw mutant (Figure 6H). This change in dynamics by two orders of magnitude suggests that if

hydrophobicity and electrostatics can roughly compensate for each other to promote effective targeting of AHs to LDs, only a precise distribution of charged residues can lead to the exceptional stability that is observed for Plin4 AH at the LD surface.

Finally, we tested the interaction of purified csw 12mer with oil. Like Plin4 AH, csw 12mer could produce oil droplets in our vortexing assay (Figure 7A). However, the droplets formed with csw 12mer were significantly larger by DLS (Figure 7B). When we added Alexa488-labelled Plin4 12mer to preformed csw-12mer-oil droplets, we observed a significant incorporation of Alexa-488 fluorescence into the droplets (Figure 7C,D), in contrast to the lack of exchange observed between non-fluorescent and fluorescent Plin4 12mer (Figure 5E,F). Therefore, mutations in the polar side of Plin4 AH that reorganized its charged residues led to a large decrease in the stability of Plin4 AH interaction with lipid particles or LDs and a concomitant increase in particle size, in agreement with our cellular data.

Model of Plin4 helix on lipid surface

Based on differences in the behavior of Plin4 and other perilipin AHs and the results obtained with Plin4 AH mutants, we hypothesize that the particular aa distribution in the polar face of the Plin4 AH enables formation of a highly stable helical lattice on a lipid surface. To test this model, we first analyzed the structure of Plin4 AH on the surface of protein-oil particles formed *in vitro*. For this aim, we purified Plin4 12 mer-oil particles by centrifugation through a sucrose gradient before subjecting them to analysis by CD spectroscopy (Figure 8A). Despite high noise due to the turbidity of the sample, the Plin4 12 mer-oil suspensions yielded spectra typical of α -helices, with a signature peak at 222 nm. Moreover, the ellipticity signal, which depends on protein concentration, compared well with that of pure Plin4 12 mer solution with TFE within the estimated concentration range (Figure 8A). These experiments indicate that on the surface of oil, Plin4 AH folds into a helix, as also observed with the helix-inducing agent TFE or with liposomes containing diphytanoyl phospholipids (Copic et al., 2018).

Our model predicts that the AHs should be densely and uniformly packed to enable short-range lateral interactions between specific polar/charged residues. To assess the density of Plin4 helices on the surface of oil particles, we compared the surface fluorescence of Plin4-oil particles, which was very uniform (Figure 8B), with that of Plin4 on bead-supported bilayers

(Figure 8C,D). We used bead-supported bilayers (Pucadyil and Schmid, 2010) containing diphytanoyl phospholipids, to which Plin4 AH readily binds (Copic et al., 2018). These beads are highly uniform in size, can be easily imaged and their sedimentation facilitated bulk measurements of the partitioning of Plin4, allowing us to standardize Plin4 12mer-A488 fluorescence per protein surface density. When the beads were added to a solution of 20 - 100 nM fluorescent Plin4 12mer at a lipid to protein molar ratio of 200 to 1000, they acquired within minutes a largely uniform fluorescent signal on their surface, which was stable over time (Figure 8C). By measuring total fluorescence in solution before and after incubation with beads, we determined the fraction of total Plin4 bound to beads (Supplementary Table 2). The amount of fluorescent signal on the beads increased roughly linearly with Plin4 12mer concentration or with the concentration of fluorescent protein when we varied the ratio of fluorescent to non-fluorescent Plin4 12mer, and decreased roughly linearly with increasing number of beads (Figure 8D). We used the measurements of average surface fluorescence on beads at five different Plin4-to-bead ratios to calculate the fluorescence per surface Plin4 concentration. Comparing the surface fluorescence on bead-supported bilayers with surface fluorescence of Plin4-oil particles, we estimated the density of Plin4-12mer on oil at around 0.07 molecule/nm², i.e, one molecule occupying an area of around 15 nm². This is close to the predicted size of a 3-11 helix 396 aa in length with the structure like the AH of α -synuclein (Jao et al., 2008), which would occupy an area of 30 nm² (0.5 nm x 0.15 nm x 396 aa); therefore, tight packing of such molecules falls within the range of our measurement.

We also note that the fluorescence of Plin4 12mer on oil was about 10-fold higher than the fluorescence that we could achieve on bead-supported bilayers at the same fluorescent protein dilution (1:20; see Figure 8B-D). At higher protein concentrations, the Plin4 AH fluorescence on beads became highly uneven, suggesting formation of domains and distortion of the bilayer (Figure 8C, bottom image). This was reminiscent of the behavior of α -synuclein on liposomes of a similar composition (Garten et al., 2015). We therefore conclude that Plin4 AH can achieve a higher density of packing on the surface of neutral lipids than in the presence of phospholipids.

We can summarize our data with a model presented in Figure 8E. Plin4 AH, as well as other perilipin AHs, is unfolded in solution / the cytosol. In contact with a hydrophobic lipid surface, they fold into a helix, whose apolar side engages in hydrophobic interactions with the

496 lipid surface. Due to the low hydrophobicity of these AHs, these interactions are weak, and
497 yet sufficient for targeting LDs due to the high length of perilipin AHs. In the case of Plin4,
498 the helices have a high propensity to interact via polar/charged side-chains, thus forming a
499 highly stable coat on the lipid surface.

500

501

Discussion

Perilipins are among the most abundant proteins in the LD proteomes (Brasaemle et al., 2004; Sztalryd and Brasaemle, 2017). Whereas their importance for LD metabolism has been known for a long time, notably for the recruitment of lipases and their inhibitors, this does not explain their abundance on the LD surface. The role of Plin4, by far the largest of perilipins, has been particularly puzzling. Plin4 is a mammalian-specific protein and is highly expressed in adipocytes (Wolins et al., 2003). Its deletion in a mouse model has so far not revealed any strong phenotypes (Chen et al., 2013). However, the striking features of Plin4 AH in terms of its length, repetitiveness and particular aa composition suggest a strong selection for a specific function. Our experiments show that the interaction of Plin4 AH with LDs *in vitro* and in cellular model systems is remarkably stable. The slow lateral diffusion and the very slow dissociation of Plin4 AH molecules at the LD surface as assessed by FRAP, by microfluidics, or by exchange assays, are reminiscent of the behavior of vesicular coat components that polymerize on a membrane surface via lateral interactions (Saleem et al., 2015; Sorre et al., 2012).

We previously showed that the extreme length and the low hydrophobicity of Plin4 AH contributed to the specificity of its LD targeting (Copic et al., 2018). Large residues such as F or W are rare or absent in the Plin4 AH sequences, whereas three small hydrophobic residues, V, T and A, are extremely abundant (Figure 3B and Figure 8). Mutations that slightly increased hydrophobicity ($T > V$) made Plin4 promiscuous for other organelles besides LDs, whereas mutations that slightly decreased hydrophobicity ($T > S$) made Plin4 cytosolic. We now show that the Plin4(4T>S) mutant is also unable to emulsify oil *in vitro* although it binds to an exposed oil surface in microfluidics experiments. Thus, the hydrophobicity of Plin4 AH appears at the threshold of promoting LD binding. Our experiments in the yeast model (Figure 3C-E) show that this is also the case for other perilipin AHs, consistent with their overall similar chemistries. A slight exception is the AH of Plin1, which contains some aromatic residues and partitions to LDs better than other AHs (Rowe et al., 2016; Ajjaji et al., 2019). Overall, the hydrophobicity of perilipin AHs appears at best modest and generally extremely low. As such, these proteins challenge a recent model for AH-LD interaction in which the main driving force is the intercalation of bulky hydrophobic residues within lipid packing defects at the LD surface (Prévost et al., 2018). This model derives from binding experiments and cellular observations performed with AHs that are much shorter than those

of perilipins and bind not only to LDs but also other organelles (e.g. ALPS motif, CCT α , Arf1). As such, this model does not account for the particular chemistry of Plin AHs, which are the most abundant and specific AHs of LDs.

Surprisingly, the polar face of Plin4 AH makes a very large contribution to LD targeting. The sequence conservation in this face, including a strong preference for K over R and D over E, suggests that polar and charged residues play an important role. All mutations that we tested, including N>Q, Q>N, K>R and D>E, decreased Plin4 AH LD targeting, with the first three mutations almost completely preventing LD binding. Furthermore, merely changing the distribution of these residues in the polar face led to a reduction in LD targeting and in stability of binding to triolein droplets *in vitro*. We thus propose that binding of Plin4 AH is controlled by the numerous electrostatic/hydrogen interactions that its polar side chains can engage in along its gigantic length. These features speak in favor of a ‘coat’ model: numerous Plin4 molecules held together by side-side interactions would form a network at the LD surface. A prediction of this model is that Plin4 should be immobilized at the LD surface and, thereby, should exhibit very limited dynamics. This was confirmed by our experiments, which revealed a drastic difference between Plin4 AH and other perilipin AHs in cells and *in vitro*. Furthermore, we showed that Plin4 AHs were densely packed on the surface of oil particles, in agreement with our model. Both on LDs in cells and with oil particles formed *in vitro*, Plin4 AH imposed a smaller size on these structures compared to other perilipin AHs or the csw mutant; therefore, stable binding of Plin4 AH correlated with smaller LD size. Interestingly, endogenous Plin4 was observed localizing to small LDs in cultured adipocytes, in contrast to Plin1 (Wolins et al., 2003).

The coat model of Plin4 is reminiscent of the interactions that apolipoproteins engage in to form secreted lipoprotein particles (Phillips, 2013). ApoA1, for which most structural information is available, forms a ring around the lipid core in low density lipoprotein particles, stabilizing itself via interactions between charged residues from two adjacent molecules (Bibow et al., 2017; Pourmousa et al., 2018; Melchior et al., 2017). 26 intermolecular salt-bridges connect two antiparallel rings of ApoA1, which is about 200 aa long. The abundance of positively (3) and negatively (2) charged residues in each 33-aa repeat of Plin4 is compatible with the formation of a similar large network of intra or intermolecular interactions. Interestingly, this model does not impose a strict geometry for the protein network. The large number of glycine residues in Plin4 AH (5 G per 33-aa repeat)

could enable the formation of various turns, resulting in a spaghetti-like layer rather than a geometrically well-defined assembly.

The observation that perilipins decorate different LDs in the same cell type supports our model of a higher-order perilipin organization (Hsieh et al., 2012; Wolins et al., 2005). The network of electrostatic interactions between perilipin AHs should be strongly dependent on their exact sequences, making the formation of hybrid coats with different perilipins less likely than homogenous perilipin coats. However, what drives the sequential coating of LDs by different perilipins remains mysterious. In addition to their repetitive AH regions, other segments of Plin1, Plin2 and Plin3 have been implicated in binding to LDs, in particular the C-terminal 4-helix bundle (Subramanian et al., 2004; Mirheydari et al., 2016; Ajjaji et al., 2019), but this has not been the case for Plin4 (Copic et al., 2018). In contrast to the behavior of their AHs, the association of full-length Plin1 and Plin2 with LDs can be very stable (Targett-Adams et al., 2003; Soni et al., 2009; Pataki et al., 2018; Ajjaji et al., 2019), and the COPI machinery has been implicated in the recruitment of Plin2 to LDs by an unknown mechanism (Nakamura et al., 2004; Soni et al., 2009).

Whereas vesicular coats uniformly cover the surface of vesicles, this is unlikely to be the case for perilipin coats. Non-uniform distribution of Plin1 on LD surface has been observed in cultured adipocytes (Blanchette-Mackie et al., 1995; Hansen et al., 2017); this can be explained by a coating model, where patches of laterally-interacting perilipin coat might coexist with LD regions decorated by other proteins. More generally, deciphering the molecular arrangements of Plin4 molecules or other perilipins on LDs is a considerable challenge for the future. In the case of apolipoproteins, a consensual model for their organization is just starting to emerge despite decades of intense investigations on these proteins.

The sequence of Plin4 is particularly striking in light of a recent study that identified an increased number of homologous repeats (10 additional repeats) in the Plin4 AH encoding region of individuals from a single family with a rare muscular degeneration (Ruggieri et al., 2020). The study proposes that a higher number of repeats in Plin4 leads to protein aggregation in muscle cells, suggesting that the sequence of Plin4 represents a risk for the organism. It is then even more surprising that a protein with such a long and repetitive AH has arisen during the mammalian evolution. While our results suggest that such a configuration

represents a means of guarding the stability of LDs, the precise advantages for mammalian cellular metabolic pathways remain to be discovered.

Key Resources Table

Reagent type (species) or resource	Designation	Source or reference	Identifiers	Additional information
gene (<i>Homo sapiens</i>)	PLIN1	Jacquier et al., 2013	PLIN1_HUMAN AAH31084.1	Suppl. Table 1
gene (<i>Homo sapiens</i>)	PLIN2	Jacquier et al., 2013	PLIN2_HUMAN AAH05127.1	Suppl. Table 1
gene (<i>Homo sapiens</i>)	PLIN3	Jacquier et al., 2013	PLIN3_HUMAN AAC39751.1	Suppl. Table 1
strain, strain background (<i>Escherichia coli</i>)	BL21(DE3)	ThermoFisher	C600003	Chemically competent cells
strain, strain background (<i>Saccharomyces cerevisiae</i>)	BY4742	<i>Euroscarf</i>	MAT α <i>his3Δ1 leu2Δ0 lys2Δ0 ura3Δ0</i>	
strain, strain background (<i>S. cerevisiae</i>)	<i>pet10Δ</i>	<i>Euroscarf</i>	MAT α <i>his3Δ1 leu2Δ0 lys2Δ0 ura3Δ0 pet10Δ::KANMX4</i>	
strain, strain background (<i>S. cerevisiae</i>)	Pet10-GFP	Huh et al., 2003	MAT α <i>his3Δ1 leu2Δ0 lys2Δ0 ura3Δ0 PET10-GFP::HisMX</i>	
cell line (<i>D. melanogaster</i>)	S2	ThermoFisher	R69007	
cell line (<i>Homo-sapiens</i>)	HeLa	ATCC	CCL-2	

Antibody	anti-GFP (rabbit polyclonal)	Thermo Fisher Scientific	A11122	(1:5000)
Antibody	anti-rabbit (goat polyclonal, HRP conjugate)	Sigma-Aldrich	A6154	(1:5000)
Antibody	anti-Vps10 (mouse monoclonal)	Molecular probes	A-21274	(1:100)
Antibody	anti-mouse (donkey, HRP conjugate)	GE Healthcare	NA934V	(1:10000)
peptide, recombinant protein	Plin4 12mer	Copic et al., 2018	Human Plin4 (aa510-905)	Suppl. Table 2
peptide, recombinant protein	Plin4 4mer	Copic et al., 2018	Human Plin4 (aa246-377)	Suppl. Table 2
peptide, recombinant protein	Plin4(4T>S) (4mer)	This study		Suppl. Table 2
peptide, recombinant protein	Plin4(NN) (4mer)	This study		Suppl. Table 2
peptide, recombinant protein	Plin4 csw (12mer)	This study		Suppl. Table 2
peptide, recombinant protein	Plin3 AH	This study	Human Plin3 (aa113 – 205)	Suppl. Table 2
chemical compound, drug	SyproOrange	ThermoFisher	S6651	

chemical compound, drug	Alexa488 C5 maleimide	ThermoFisher	A10254	
chemical compound, drug	Alexa568 C5 maleimide	ThermoFisher	A20341	
chemical compound, drug	Bodipy 493/503	ThermoFisher	11540326	
chemical compound, drug	diphytanoyl-phosphatidylserine	Avanti Lipids	AVA-850408C-25Mg	
chemical compound, drug	diphytanoyl-phosphatidylcholine	Avanti Lipids	AVA-850356C-200Mg	
other	Glass microfluidic chip with a T-junction	Dolomite	part # 3000086	
other	Glass microfluidic chip with a T-junction	Dolomite	part # 3000024	
other	Silica Microspheres, 5.00µm, SS05N	Bang laboratories	SS05003-0.5	

609

610 **Materials and Methods**

611 **Sequence analysis**

612 The 11-aa repeats of perilipins were identified using HHrepID tool from the MPI
613 Bioinformatics Toolkit server (Biegert and Söding, 2008; Zimmermann et al., 2018). The
614 amphipathic character of these sequences was analysed using HeliQuest (Gautier et al., 2008).
615 Helical wheels were plotted as complete 3–11 helices; the presentation of helices was chosen
616 such as to maximise their hydrophobic moment, as calculated by Heliquest, and inclusion of
617 identified 11-aa repeats, excluding helix-breaking proline (Pace and Scholtz, 1998) from the
618 middle of the helices. The amino acid conservation of the 33-aa repeats of Plin4 was
619 represented using Weblogo (Crooks et al., 2004).

620

621 **Plasmid DNA construction**

622 All plasmids used in this study are listed in Table 1. DNAs encoding AHs of human Plin1,
623 Plin2 and Plin3 were PCR-amplified from the corresponding cDNAs that had been cloned
624 into pGREG576 plasmids (gift from R. Schneiter, U. of Fribourg) (Jacquier et al., 2013).
625 DNA for Plin4 6mer and Plin4 8mer was amplified from plasmid pCLG26, and DNA for
626 Plin4 4mer mutant 4T>S was amplified from plasmids pSB49 (Copic et al., 2018). Plin4 4mer
627 mutants (2D>E, 3K>3, NN, QN and QQ), and Plin4 12mer mutant csw 12mer were
628 constructed using synthetic double-stranded DNA fragments (Supplementary table 1). All
629 4mer mutants were exact 4x repeats of a 33-aa sequence, based on the parental sequence of
630 human Plin4 fragment aa246-278. The protein sequence for csw 12mer was designed by
631 manually adjusting 33-aa helical wheels of the parental Plin4 12mer sequence using
632 HeliQuest to increase the symmetry of charged residue distribution in the polar side of the
633 helix while minimizing changes in the hydrophobic moment. DNA sequences were optimized
634 for synthesis using the algorithm on the Eurofins website (<https://www.eurofinsgenomics.eu>).
635 Supplementary table 2 also lists all protein sequences used in this study.

636 For expression of proteins in *E. coli*, PCR-amplified DNA fragments were inserted into
637 pET21b (Novagen) without adding a tag using *NheI* and *XhoI* restriction sites, which were
638 introduced by PCR. For expression of Plin3 AH, an additional sequence ‘MASC’ was
639 introduced upstream of the AH.

640 For expression of GFP fusion proteins in *S. cerevisiae*, PCR-amplified DNA fragments were
641 inserted into pRS416-derived (URA3 and AmpR markers) CEN plasmid pRHT140 containing

ADH1 promoter and GFP for C-terminal tagging (gift from S. Leon, IJM). For expression of mCherry fusion proteins, GFP-encoding fragment in this vector was replaced with mCherry using *KpnI* and *BamHI* restriction sites to generate plasmid pMGA4. All AH DNA fragments were cloned into these plasmids using *NheI* and *BamHI* restriction sites that were introduced by PCR. The sequence of the multiple cloning site introduces a linker peptide in the resulting fusion protein between the AH and GFP, ‘PLDPPGLQEF’, and linker peptide ‘VKDPDIKLID’ between the AH and mCherry.

Plasmids for expression of mCherry fusion proteins in HeLa cells were constructed by subcloning synthetic genes for Plin4 mutants into pmCherry-N1 (Invitrogen) using *BamHI* and *XhoI* restriction sites. All plasmids were verified by sequencing.

Protein purification

All proteins were purified from *E. coli* without a tag. Plin4 12mer and Plin4 4mer were purified as previously described (Copic et al., 2018). Plin3 AH (aa103 to 205), Plin4 4T>S, Plin4 NN, and csw 12mer were purified following a similar protocol, with some modifications in the case of Plin 3 AH, as outlined below. *E. coli* cells BL21DE3 transformed with expression plasmids were grown to O.D. \approx 0.6 at 37°C from a liquid preculture and induced with 1 mM IPTG for 1 h at 37 °C. Cells from 0.25 l cultures were collected by centrifugation and frozen. The bacterial pellets were thawed in lysis buffer (50 mM Tris-HCl pH 7.5, 150 mM NaCl, 1 mM DTT, supplemented with 0.1 mM PMSF, and Complete protease inhibitor cocktail (Roche)). Cells were broken by sonication. The lysate was centrifuged at $100,000 \times g$ for 30 min at 4°C in a 70.1Ti Rotor (40,000 rpm; Beckman). The supernatant in centrifuge tubes was immersed in boiling water (95°C) for 30 min. The resulting cloudy suspension was centrifuged at $100,000 \times g$ for 15 min at 4°C to remove precipitated material. The supernatant was dialyzed against 20 mM Tris-HCl pH 7.5, 10 mM NaCl, 1 mM DTT at 4 °C using Spectra/Por membranes with a cut-off of 6000 Da (Spectrum labs) and then centrifuged again at $100,000 \times g$ for 30 min at 4 °C. Plin4 4T>S and csw 12mer were then further purified in a single step by cation exchange chromatography on a 20 ml Hiprep S HP column (GE Healthcare), as described for Plin4 AHs (Copic et al., 2018). Plin4 NN was dialyzed against 20 mM MES-HCl pH 5.5, 10 mM NaCl, 1 mM DTT before cation exchange chromatography and eluted with a salt gradient from 10 mM to 400 mM (3 column volumes) in MES buffer. Purified Plin4 NN was then dialyzed against 20 mM Tris-HCl pH 7.5, 100 mM NaCl, 1 mM DTT using a Slide-A-Lyzer dialysis cassette (Thermo Scientific) with a cut- off of 2000 Da. In contrast to Plin4 AH, Plin3 AH has a net negative charge at

neutral pH (pI = 4.65). Therefore, Plin3 AH was purified by anion exchange chromatography on a 20 ml HiPrep Q HP column (GE Healthcare). It was eluted with a salt gradient from 10 mM to 400mM NaCl (3 column volumes) in 20 mM Tris-HCl pH 7.5, 1 mM DTT at a flow rate of 2 ml/min using an Akta purifier system (GE Healthcare), eluting at approximately 100 mM NaCl. After analysis of the chromatography fractions by protein electrophoresis, the protein pools were divided in small aliquots and stored at -80°C .

Protein electrophoresis and determination of protein concentration

Standard Glycine SDS-PAGE was used for the analysis of Plin4 12mer and csw 12mer (Mw ~ 40 kDa) using homemade 13% acrylamide-bisacrylamide gels. Tricine SDS-PAGE (Schägger and Jagow, 1987) was used for proteins with lower molecular weight, i.e. Plin4 4mer, Plin4 4T>S, Plin4 NN, or Plin3 AH (9 – 15 kDa). For that we either used TruPAGE commercial gels (Sigma) and homemade Tris-MOPS buffer (60 mM Trizma, 30 mM 4-Morpholinepropanesulfonic acid (MOPS), 0.1% w/v SDS), or, for better resolution, homemade 16.5% acrylamide-polyacrylamide (29:1) gels run with tricine buffer (100 mM Tris-HCl pH 8 – 8.5, 0.1 M Tricine, 0.1% SDS) in the cathode and 200 mM Tris HCl pH 8.9 in the anode chamber. Gels were rinsed in 7.5% acetic acid, stained with SyprOrange (Life Technologies) and visualized with a MP imaging system (Bio-Rad) using the Alexa 488 settings. Because all perilipin AH purified construct lack aromatic residues, preventing protein quantification by UV spectroscopy or by Bradford assay, protein concentration was routinely determined by densitometry of Sypro-Orange or Coomassie Blue stained gels against a calibration curve with protein standards (Sigma) using ImageJ. Quantification by gel electrophoresis was verified by Ellman's reaction method as previously described (Copic et al., 2018).

Protein labelling with fluorescent probes

Purified AHs were covalently labelled via cysteines using Alexa C5 maleimide probes (either 488 or 568; Thermofisher). Plin4 12mer, Plin4 4mer and Plin4 4T>S were labelled on endogenous cysteines present in their AHs; they all contain 4 cysteines in total. Plin3 AH is devoid of cysteines, therefore a single cysteine was introduced at its N-terminus. To remove DTT, 1 ml of protein solution at concentration 0.7 mg/ml (18 μM of Plin4 12mer and csw 12mer, 50 μM of Plin4 4mer and Plin4 4T>S) was exchanged into labelling buffer (20 mM Tris-HCl pH 7.5, 100 mM NaCl) using size exclusion NAP10 columns (GE Healthcare). Protein-containing fractions were identified by protein electrophoresis and pooled. Protein

solutions were incubated for 5 minutes at 4 °C with Alexa C5 maleimide probes at an equimolar ratio to their total number of cysteines (1 ml reaction volume). The reactions were stopped by the addition of DTT to 10 mM final concentration and loaded on NAP10 columns to separate the labelled protein from the excess of fluorescent probe. Fractions were analysed by protein electrophoresis. Fluorescence in the gel was directly visualized on ChemiDoc MP imaging system (Bio-Rad) either with Alexa 488 or SyproRuby (for Alexa 568) settings. Fractions with labelled protein were pooled, aliquoted and stored at -80°C. The same protocol was used for labelling of free cysteine, but without NAP10 purification steps.

We used FRAP assays on protein-oil emulsions (see below) with different ratios of labelled to unlabelled proteins to verify that the fluorescent label did not change the behaviour of the protein. This was not the case for labelled Plin3 AH, thus we only used this protein in unlabelled form in our biochemical assays.

Preparation of protein-oil emulsions

Proteins were diluted to 0.5 mg/ml in freshly degassed HKM buffer (50 mM Hepes-KOH pH 7.2, 120 mM K-acetate, 1 mM MgCl₂) supplemented after degassing with 1 mM DTT. 190 µl of each solution were pipetted into a 600 µl glass tube, and a 10 µl drop of triolein (>99% purify, T7140 Sigma) was added to the top. In some cases, emulsions were prepared to have a final volume of 100 µl and the drop of triolein was 5 µl. They were vortexed manually at a fixed angle of ~30° for three cycles of 30 s on 30 s off at 25 °C under argon atmosphere. Images of resulting emulsions were taken with a compact camera. For analysis by fluorescent microscopy, emulsions were prepared using a mixture of fluorescent and unlabelled protein at a mass ratio 1:20 for Plin4 12mer and 4T>S, and 1:50 for Plin4 4mer.

Dynamic Light Scattering (DLS)

Measurements of the mean hydrodynamic radius of the Plin4-oil droplets by dynamic light scattering were performed on a sample taken from the middle of the tube, avoiding any unreacted oil that remained at the top of the emulsion, at least 3 h after vortexing to prevent the interference of gas bubbles with the measurement. Subsequent samples at later time points were removed in the same manner without any additional mixing. Emulsion samples were diluted 100-fold in freshly degassed HKM buffer with 1mM DTT. Measurements were performed on a Zetasizer Nano ZS machine (Malvern) at 25°C, and data were processed using the CONTIN method.

Observation of protein-oil interaction using microfluidics

Microfluidic experiments were performed in a glass microfluidic chip with a T-junction geometry purchased from Dolomite (part # 3000086 and 3000024). All channels had a rounded cross-section with a 100 μm height and a 110 μm width. Prior to the measurements, the channel walls were wetted with 100 μl of freshly degassed HKM buffer supplemented with 1 mM DTT. The flows were driven and precisely controlled using a piezoelectric pressure control system (OB1 MK3, Elveflow), with typically applied pressures below 300 mbar. After wetting, the main and side inlet channels were filled with buffer and triolein (Sigma), respectively. Injection of oil in the side inlet channel was gently stopped with a manual valve (MV201, LabSmith) before the oil reached the junction (when the meniscus was approximately 400 μm from the junction). In this way, the flow in the main inlet channel could be stopped without significantly affecting the meniscus of oil, and the inlet vial with buffer could be exchanged by a vial with fluorescent protein solution (0.1 mg/ml in HKM buffer, mixed at a ratio 10 : 1 for unlabelled vs Alexa488-labelled protein). The sample volume in the vial was approximately 400 μl . The flow in the main inlet channel was then resumed and the diffusion of the protein from the main inlet channel into the side channel and its adsorption onto oil meniscus was monitored by time-lapse confocal microscopy for up to 30 min at a rate of 1 frame every 3 seconds (ECLIPSE TE2000-E, Plan Fluor 40x objective, EZC1 software, Nikon). Finally, the flow in the main inlet channel was stopped again, the inlet vial exchanged by a vial with buffer, and the main inlet channel was rinsed while monitoring the diffusion of the protein from the side channel. For competition experiments between Plin4 12mer and 4T>S mutant, proteins were mixed at a mass ratio 50:1 for unlabelled to labelled protein, Plin4 12mer: Plin4 12mer-Alex488 or 4T>S: Plin4 12mer-Alex488, with a total protein concentration of 0.1 mg/ml. All experiments were conducted at room temperature. Between experiments, glass chips were regenerated by copious washing with 3% SDS at 50°C, followed by distilled water, 3% TFD4 at 50°C, distilled water and finally dried by air (except for the measurements of the surface tension, where inhomogeneous glass surface was needed to increase the contact angle hysteresis). Image analysis was performed with ImageJ/Fiji (Schindelin et al., 2012) and Matlab.

Separation of Plin4-oil emulsion on sucrose gradients

Emulsions were prepared as specified in a final volume of 300 μl including 15 μl of triolein and 0.5 mg/ml of protein. Next, 240 μl of 60% w/v solution of sucrose in HKM buffer with 1 mM DTT was mixed with 240 μl of emulsion, avoiding any oil. 450 μl of this suspension was

loaded on the bottom of a centrifuge tube and overlaid with a step sucrose gradient consisting of 300 μ l 20%, 300 μ l 10% and 100 μ l 0% sucrose in HKM buffer with 1mM DTT. The samples were centrifuged at 50,000 rpm ($214,000 \times g$) in a Beckman swing-out rotor (TLS 55) for 80 min at 8°C. Four fractions were carefully collected from the bottom with a Hamilton syringe, having the following volumes: 450 μ l, 300 μ l, 300 μ l, and 100 μ l, respectively. Equal volumes of all fractions were analysed by protein electrophoresis.

Circular dichroism

CD measurements were conducted on a Jasco J-815 spectrometer at room temperature with a quartz cell of 0.05 cm path length. For the comparison between wild type and mutant Plin4 in buffer (10 mM Tris, pH 7.5, KCl 150 mM) or in buffer + 50% trifluoroethanol (TFE), the spectrum was obtained by averaging 6 scans recorded from 195 to 260 nm (bandwidth: 1 nm; step size: 0.5 nm; scan speed: 50 nm/min). Ellipticity was converted to mean residue ellipticity (MRE) by dividing by the product of protein concentration, residue number and path length distance. For the CD spectra of Plin 12mer on oil, emulsions were purified on sucrose gradients in 10 mM Tris, pH 7.5, KCl 150 mM with 0.1 mM DTT and the top 100 μ l fraction was collected and placed in the CD cuvette. The spectrum was obtained by averaging 20 scans recorded from 200 to 260 nm (bandwidth: 1 nm; step size: 0.5 nm; scan speed: 20 nm/min). The Plin4 standards were run with these settings. CD spectra were smoothened with the means-movement method with a convolution width of 5.

Binding of Plin4 to bead-supported bilayers

We prepared bead-supported bilayers using 5 μ m silica beads (Bang laboratories) and extruded liposomes composed of 50% diphytanoyl-phosphatidylserine and 50% diphytanoyl-phosphatidylcholine (Avanti Lipids) (Copic et al., 2018) as described (Pucadyil and Schmid, 2010). 200 μ M liposomes were incubated with 25×10^6 beads in 500 μ L of HKM buffer for 30 min at room temperature under gentle agitation, and washed three times in HKM buffer with low-speed centrifugation ($200 \times g$ for 2min). To bind fluorescent Plin4 12mer to bead-supported bilayers, freshly-prepared beads were incubated with a mixture of Plin4 12mer and Plin4 12mer-A488 in 30 μ L in HKM buffer for 15 min at room temperature, after which the beads were imaged directly by fluorescence microscopy. Alternatively, the fluorescence of the solution before and after incubation was measured in a 96-well opaque plate using a Spectramax M2 fluorimeter (Molecular devices) (excitation 488, emission 525 nm).

Yeast growth and media

Yeast strains used were: BY4742 MAT α *his3 Δ 1 leu2 Δ 0 lys2 Δ 0 ura3 Δ 0* (Euroscarf), BY4742 *pet10 Δ ::KANMX4* (Euroscarf), and BY4741 MAT α *his3 Δ 1 leu2 Δ 0 met15 Δ 0 ura3 Δ 0 PET10-GFP::HisMX* (Huh et al., 2003). Yeast were transformed by standard lithium acetate/polyethylene glycol procedure. Yeast cells expressing different AH constructs were grown in synthetic complete medium lacking uracil (SC-Ura, 6.7 g/l yeast nitrogen base, amino acid supplement without uracil, 2% glucose). To induce LDs, yeast cells either grown in SC-Ura for 24h at 30°C (stationary phase) or for 24h in SC-Ura, followed by 24h incubation in oleic acid (OA) medium (0.67% yeast nitrogen base without amino acids, 0.1 % yeast extract, 0.1 % (v/v) oleate, 0.25 % (v/v) Tween 40, amino acid supplement lacking uracil). For imaging of LDs in early stationary phase, yeast cells were inoculated from a preculture and grown at 30°C in SC-Ura to a final OD₆₀₀=1-2.

Preparation of yeast protein extracts and western blot analysis

Yeast cultures were grown overnight in SD-Ura medium to mid- logarithmic phase. Proteins were extracted from one OD₆₀₀ equivalent of cells by Li-acetate/alkaline extraction as described (Zhang et al., 2011), resuspended in 100 μ l of sample buffer (50 mM Tris-HCl, pH 6.8, 100 mM DTT, 2% SDS, 0.1% Bromophenol Blue and 10% glycerol), heated at 65°C for 10 min, and 10 μ l was loaded on SDS-PAGE (4–20% Mini-PROTEAN TGX Stain-Free, Bio-Rad). After electrophoresis, total proteins were visualized in the TGX Stain-Free gels (Bio-Rad) after 1 min UV-induced photoactivation with a Gel Doc EZ Imager (Bio-Rad). Proteins were transferred onto a nitrocellulose membrane and perilipin AH-GFP fusions were detected with a rabbit polyclonal anti-GFP antibody (Thermo Fisher Scientific, A11122, 1:5000 dilution). Vps10, when was used as a loading control, was detected with mouse anti-Vps10 monoclonal antibody (Molecular probes, A-21274, 1:100 dilution). Horseradish peroxidase-coupled anti-rabbit (Sigma-Aldrich, A6154) and anti-mouse (GE Healthcare, NA934V) secondary antibodies were used at 1:5000 dilution. Chemiluminescence signals were acquired using Gel Doc EZ Imager.

Cell culture and transfection

HeLa cells (ATCC) were grown in Dulbecco's modified Eagle's medium (DMEM) supplemented with 4.5 g/l glucose (Life technologies), 10% fetal bovine serum (FBS, Life

technology) and 1% Penicillin/Streptomycin antibiotics (Life technologies). All cell cultures were routinely verified to be free of Mycoplasma by DAPI stain on fixed permeabilized cells. For protein expression, subconfluent cells were transfected with Lipofectamine 2000 (Invitrogen) in Optimem medium (Life technologies) for 6 h, followed by 16 h in standard growth medium before the cells were fixed and prepared for imaging. Drosophila S2 cells (ThermoFisher) were cultured in Schneider's Drosophila medium (Invitrogen) supplemented with 10% FBS and 1% Penicillin/Streptomycin at 25°C. For generating stably-transfected cells, cells were incubated with plasmid DNA and TransIT-Insect Reagent (Mirus), followed by selection with 2 µg/ml puromycin (Life technologies) for 2 weeks. Protein expression from the metal-inducible promoter was induced for 48 h with the addition of 100 µM Cu-sulfate to the medium. Lipid droplets were induced with 1 mM oleic acid (Sigma) in complex with fatty-acid free BSA (Sigma) for 24 h. RNAi depletion against CCT1 was performed as described (Copic et al., 2018).

Fluorescent microscopy

For imaging of purified protein-oil emulsions, emulsions prepared with fluorescent protein were gently mixed in the glass tube before 1.5 µl of emulsion was withdrawn with a long 200 µl tip and placed on an untreated glass slides (Thermo Scientific). A coverslip was carefully placed on top without applying any pressure. Proteins on bead-supported bilayers were imaged in the same manner.

Yeast cells were harvested by centrifugation, washed, placed on a glass slide and covered with a coverslip. For some experiments, LDs were stained with 1 µg/ml Bodipy 493/503 (Life Technologies) or with Autodot blue dye (Clinisciences) diluted 1000-fold for 30 min at room temp, after which the cells were washed twice and imaged. Drosophila S2 cells were imaged on glass slides in the same way as yeast cells.

Transfected HeLa cells were fixed with 3.2% paraformaldehyde (Sigma) in PBS for 30 min at room temp. After washing three times with PBS, cells were stained with Bodipy 493/503 at 1 µg/ml for 30 min at room temperature and washed three times with PBS. Cells were mounted on coverslips with Prolong (Life technologies).

Images of emulsions, bead-supported bilayers, yeast and S2 cells were acquired at room temperature with an Axio Observer Z1 (Zeiss) microscope, equipped with an oil immersion plan-Apochromat 100x/1.4 objective, an sCMOS PRIME 95 (Photometrics) camera, and a spinning-disk confocal system CSU-X1 (Yokogawa) driven by MetaMorph software (Molecular Devices). GFP-tagged or Alex488-labelled proteins and mCherry-tagged or

Alex568-labelled proteins were visualized with a GFP Filter 535AF45 and an RFP Filter 590DF35, respectively. When imaging emulsions, images were acquired in 10 to 15 z-sections of 0.2 μm were taken. For imaging HeLa cells and quantification of LD-to-PM signal ratio in yeast, we used an LSM 780 confocal microscope (Zeiss) with a x63/1.4 oil objective and a PMT GaAsP camera, driven by ZEN software. Images were processed with ImageJ and prepared for figures with Canvas Draw (canvas X).

Fluorescence recovery after photobleaching (FRAP)

FRAP assays *in vitro* were performed on freshly-prepared fluorescent emulsions with Alex488-labelled proteins on glass slides using the CSU-X1 spinning disc microscope and 100x objective, bleaching laser with a wavelength of 473 nm and iLas software controlled by Metamorph. Several circular areas of 25 x 25 pixels were bleached in each field (828 x 960 pixels), either on oil particles or in surrounding solution. The following FRAP time-course was used: 6 images pre-bleach, then bleach followed by 10 s of 1 image/s, 60 s of 1 image/10 s, and finally 600 s of 1 image/30 s (or until the loss of focus). Fluorescence of the bleached area at each time point was normalized to the average fluorescence before bleaching. Data was processed using Excel.

For FRAP assays in yeast cells, a circular area of 15 x 15 pixels in a cell expressing a GFP-fusion protein was bleached, either on the LDs or on the plasma membrane. 5 images were taken before bleaching, followed by a post-bleach time-course: 15 s of 1 image/s, 60 s of 1 image/5 s, and ~200 s of 1 image/20 s. Background fluorescence outside the cell was subtracted from the bleached area and the signal was normalized to the whole cell signal for each time-point. Data was processed with Excel and plotted using SigmaPlot (Systat Software).

FRAP assays in *Drosophila* S2 cells expressing Plin4 12mer-GFP were performed as for yeast, except that 3 circular areas of 15 x 15 pixels containing isolated LDs were selected per cell. The following FRAP time-course was used: 5 images pre-bleach, then bleach, followed by 30 s of 1 image/s, 60 s of 1 image/5 s, and finally ~200 s of 1 image/20 s. Data was analysed in Excel and plotted using SigmaPlot. To obtain the half-time of recovery, average curves from the 3 FRAP measurements from the same cell were fitted with an exponential-rise equation.

Protein exchange assay on protein-oil emulsions

Emulsions were prepared as described using unlabelled protein at 0.5 mg/ml and checked by

microscopy using CSU-X1 spinning disc microscope (time 0). Then, fluorescent Plin4 12mer-Alexa488 was gently added to the suspension to a final concentration of 0.025 mg/ml (20 : 1, unlabelled protein : labelled Plin4 12mer). Samples from the emulsions were withdrawn at indicated time-points without mixing and imaged on glass slides. The re-vortex sample was prepared after 2h of incubation by withdrawing 20 µl of the emulsion and vortexing it in a fresh 600 µl glass tube in the same manner as for initial emulsion preparation. Samples were imaged in 10 z-sections of 0.5 µm in randomly-selected fields of 76 µm x 101 µm. The z-section containing the highest number of small droplets was selected for analysis.

Image analysis

Images were analysed using ImageJ/Fiji (Schindelin et al., 2012). To quantify the number of droplets in protein-oil emulsions, the number of particles in a randomly-selected area in a single z-section was counted using 'find maxima' in the fluorescent channel with noise tolerance set to 100. Larger clusters were counted manually. For quantification in the exchange assay, the noise tolerance was set to 150. To quantify Plin4 surface fluorescence on bead-supported bilayers, a circle was drawn on the bead perimeter, converted to a circular line and the mean fluorescence value of the plot profile was calculated. To quantify Plin4 surface fluorescence on oil particles, a line on particles with clear dark middle and the average of the two fluorescence maxima was recorded (the two maxima varied by $6\% \pm 4\%$).

To quantify the number of yeast cells with protein signal on LDs, cells were counted manually after applying the same brightness/contrast settings to all images. To quantify the ratio of LD to PM protein signal (mCherry fusions), Pet10-GFP LD marker was used to select the regions of interest (ROIs) corresponding to LDs and the total mCherry fluorescence in the ROIs was recorded. For the quantification of PM fluorescence, images were converted to binary to select the whole yeast perimeter. Then, a band of 5 pixels was applied to include all of PM signal. After background subtraction, the total LD signal per cell was divided by the total PM signal.

LD size in yeast cells grown in oleic-acid medium was measured using the fluorescent protein. Isolated LDs were fitted manually with a perfect circle and the size of each circular area was recorder. Data were analysed in Excel and plotted with KaleidaGraph (Synergy software).

To determine the fraction of LDs in HeLa cells that were positive for transfected fluorescent protein, a single z-section that contained the most LDs in a cell was first selected. All LDs in

the selected cell section were identified in the green (Bodipy dye) channel using the ‘Analyze particle’ plug-in. LDs positive for fluorescent protein were then identified by determining a threshold value for the red fluorescent signal (mCherry-protein fusion), 1.4x above average cellular fluorescence, and counting all LDs with fluorescence above this threshold. This number was divided by the total LD number to calculate the fraction of LDs in one cell section positive for protein. Data was processed in Microsoft Excel and plotted using SigmaPlot.

Acknowledgments

We thank C. La Torre Garay, M. Tuljak, V. Countremoulins and N. Joly for technical help, and R. Schneider and S. Léon for plasmids. We acknowledge the IJM ImagoSeine facility, member of IBiSA and the France-BioImaging infrastructure (ANR-10-INBS-04), and L. Bousset, V. Albanèse, R. Gautier, J. Snoj, N. Mejhert, C. Jackson and Jackson-Verbavatz team for helpful discussions and comments on the manuscript. This work was supported by the CNRS, including a CNRS PICS grant (#214454), the Slovenian Research Agency (research core funding No. P1-0055), and ERC Synergy grant #856404. M.G.-A was supported by PhD fellowships from the French “Ministère de l’Education National, de l’Enseignement Supérieur de la Recherche” and Fondation ARC pour la recherche sur le cancer (DOC20190509052).

Competing Interests

The authors have no competing interests to declare.

973 References

- 974 Ajjaji, D., K. Ben M'barek, M.L. Mimmack, C. England, H. Herscovitz, L. Dong, R.G. Kay, S. Patel,
975 V. Saudek, D.M. Small, D.B. Savage, and A.R. Thiam. 2019. Dual binding motifs underpin the
976 hierarchical association of perilipins1-3 with lipid droplets. *Mol Biol Cell*. 30:703–716.
977 doi:10.1091/mbc.E18-08-0534.
- 978 Bacle, A., R. Gautier, C.L. Jackson, P.F.J. Fuchs, and S. Vanni. 2017. Interdigitation between
979 Triglycerides and Lipids Modulates Surface Properties of Lipid Droplets. *Biophys J*. 112:1417–
980 1430. doi:10.1016/j.bpj.2017.02.032.
- 981 Ben M'barek, K., D. Ajjaji, A. Chorlay, S. Vanni, L. Forêt, and A.R. Thiam. 2017. ER Membrane
982 Phospholipids and Surface Tension Control Cellular Lipid Droplet Formation. *Dev Cell*. 1–31.
983 doi:10.1016/j.devcel.2017.05.012.
- 984 Bersuker, K., and J.A. Olzmann. 2017. Establishing the lipid droplet proteome_ Mechanisms of lipid
985 droplet protein targeting and degradation. *BBA - Mol Cell Biol Lipids*. 1862:1166–1177.
986 doi:10.1016/j.bbalip.2017.06.006.
- 987 Bersuker, K., C.W.H. Peterson, M. To, S.J. Sahl, V. Savikhin, E.A. Grossman, D.K. Nomura, and J.A.
988 Olzmann. 2018. A Proximity Labeling Strategy Provides Insights into the Composition and
989 Dynamics of Lipid Droplet Proteomes. *Dev Cell*. 44:97–112.e7.
990 doi:10.1016/j.devcel.2017.11.020.
- 991 Bibow, S., Y. Polyhach, C. Eichmann, C.N. Chi, J. Kowal, S. Albiez, R.A. McLeod, H. Stahlberg, G.
992 Jeschke, P. Güntert, and R. Riek. 2017. Solution structure of discoidal high-density lipoprotein
993 particles with a shortened apolipoprotein A-I. *Nat Struct Mol Biol*. 24:187–193.
994 doi:10.1038/nsmb.3345.
- 995 Biegert, A., and J. Söding. 2008. De novo identification of highly diverged protein repeats by
996 probabilistic consistency. *Bioinformatics*. 24:807–814. doi:10.1093/bioinformatics/btn039.
- 997 Blanchette-Mackie, E.J., N.K. Dwyer, T. Barber, R.A. Coxey, T. Takeda, C.M. Rondinone, J.L.
998 Theodorakis, A.S. Greenberg, and C. Londos. 1995. Perilipin is located on the surface layer of
999 intracellular lipid droplets in adipocytes. *J Lipid Res*. 36:1211–1226.
- 1000 Brasaemle, D.L., G. Dolios, L. Shapiro, and R. Wang. 2004. Proteomic analysis of proteins associated
1001 with lipid droplets of basal and lipolytically stimulated 3T3-L1 adipocytes. *J Biol Chem*.
1002 279:46835–46842. doi:10.1074/jbc.M409340200.
- 1003 Bulankina, A.V., A. Deggerich, D. Wenzel, K. Mutenda, J.G. Wittmann, M.G. Rudolph, K.N. Burger,
1004 and S. Honing. 2009. TIP47 functions in the biogenesis of lipid droplets. *J Cell Biol*. 185:641–
1005 655. doi:10.1074/jbc.M402264200.
- 1006 Bussell, R., Jr, and D. Eliezer. 2003. A Structural and Functional Role for 11-mer Repeats in α -
1007 Synuclein and Other Exchangeable Lipid Binding Proteins. *J Mol Biol*. 329:763–778.
1008 doi:10.1016/S0022-2836(03)00520-5.
- 1009 Chen, W., B. Chang, X. Wu, L. Li, M. Sleeman, and L. Chan. 2013. Inactivation of Plin4
1010 downregulates Plin5 and reduces cardiac lipid accumulation in mice. *Am J Physiol Endocrinol*
1011 *Metab*. 304:E770–9. doi:10.1152/ajpendo.00523.2012.
- 1012 Chorlay, A., L. Monticelli, J.V. Ferreira, K. Ben M'barek, D. Ajjaji, S. Wang, E. Johnson, R. Beck, M.
1013 Omrane, M. Beller, P. Carvalho, and A.R. Thiam. 2019. Membrane Asymmetry Imposes

1014 Directionality on Lipid Droplet Emergence from the ER. *Dev Cell*. 1–26.
1015 doi:10.1016/j.devcel.2019.05.003.

1016 Copic, A., S. Antoine-Bally, M. Giménez-Andrés, C. La Torre Garay, B. Antonny, M.M. Manni, S.
1017 Pagnotta, J. Guihot, and C.L. Jackson. 2018. A giant amphipathic helix from a perilipin that is
1018 adapted for coating lipid droplets. *Nat Commun*. 9:1332. doi:10.1038/s41467-018-03717-8.

1019 Crooks, G.E., G. Hon, J.-M. Chandonia, and S.E. Brenner. 2004. WebLogo: a sequence logo
1020 generator. *Genome Res*. 14:1188–1190. doi:10.1101/gr.849004.

1021 Faini, M., R. Beck, F.T. Wieland, and J.A.G. Briggs. 2013. Vesicle coats: structure, function, and
1022 general principles of assembly. *Trends Cell Biol*. 1–10. doi:10.1016/j.tcb.2013.01.005.

1023 Gao, Q., D.D. Binns, L.N. Kinch, N.V. Grishin, N. Ortiz, X. Chen, and J.M. Goodman. 2017. Pet10p
1024 is a yeast perilipin that stabilizes lipid droplets and promotes their assembly. *J Cell Biol*.
1025 181:jcb.201610013–23. doi:10.1083/jcb.201610013.

1026 Garten, M., C.P.X. vost, C. Cadart, R. Gautier, L. Bousset, R. Melki, P. Bassereau, and S. Vanni.
1027 2015. Methyl-branched lipids promote the membrane adsorption of a-synuclein by enhancing
1028 shallow lipid-packing defects. *Phys Chem Chem Phys*. 1–9. doi:10.1039/C5CP00244C.

1029 Gautier, R., D. Douguet, B. Antonny, and G. Drin. 2008. HELIQUEST: a web server to screen
1030 sequences with specific -helical properties. *Bioinformatics*. 24:2101–2102.
1031 doi:10.1093/bioinformatics/btn392.

1032 Giménez-Andrés, M., A. Copic, and B. Antonny. 2018. The Many Faces of Amphipathic Helices.
1033 *Biomolecules*. 8:45. doi:10.3390/biom8030045.

1034 Granneman, J.G., V.A. Kimler, H. Zhang, X. Ye, X. Luo, J.H. Postlethwait, and R. Thummel. 2017.
1035 Lipid droplet biology and evolution illuminated by the characterization of a novel perilipin in
1036 teleost fish. *Elife*. 6:799. doi:10.7554/eLife.21771.

1037 Guo, Y., T.C. Walther, M. Rao, N. Stuurman, G. Goshima, K. Terayama, J.S. Wong, R.D. Vale, P.
1038 Walter, and R.V. Farese. 2008. Functional genomic screen reveals genes involved in lipid-droplet
1039 formation and utilization. *Nature*. 453:657–661. doi:10.1038/nature06928.

1040 Hansen, J.S., S.M. x000E9, H.A. Jones, O.G.X. ransson, and K. Lindkvist-Petersson. 2017.
1041 Visualization of lipid directed dynamics of perilipin 1 in human primary adipocytes. *Sci Rep*. 1–
1042 14. doi:10.1038/s41598-017-15059-4.

1043 Hickenbottom, S.J., A.R. Kimmel, C. Londos, and J.H. Hurley. 2004. Structure of a lipid droplet
1044 protein; the PAT family member TIP47. *Structure*. 12:1199–1207. doi:10.1016/j.str.2004.04.021.

1045 Hsieh, K., Y.K. Lee, C. Londos, B.M. Raaka, K.T. Dalen, and A.R. Kimmel. 2012. Perilipin family
1046 members preferentially sequester to either triacylglycerol-specific or cholesteryl-ester-specific
1047 intracellular lipid storage droplets. *J Cell Sci*. 125:4067–4076. doi:10.1242/jcs.104943.

1048 Huh, W.-K., J.V. Falvo, L.C. Gerke, A.S. Carroll, R.W. Howson, J.S. Weissman, and E.K. O'Shea.
1049 2003. Global analysis of protein localization in budding yeast. *Nature*. 425:686–691.
1050 doi:10.1038/nature02026.

1051 Jacquier, N., S. Mishra, V. Choudhary, and R. Schneiter. 2013. Expression of oleosin and perilipins in
1052 yeast promotes formation of lipid droplets from the endoplasmic reticulum. *J Cell Sci*. 126:5198–
1053 5209. doi:10.1242/jcs.131896.

1054 Jao, C.C., B.G. Hegde, J. Chen, I.S. Haworth, and R. Langen. 2008. Structure of membrane-bound
1055 alpha-synuclein from site-directed spin labeling and computational refinement. *Proc Natl Acad*
1056 *Sci USA*. 105:19666–19671. doi:10.1073/pnas.0807826105.

1057 Joanny, J.F., and P.G. de Gennes. 1984. A model for contact angle hysteresis. *J. Chem. Phys.* 81:552–
1058 562. doi:10.1063/1.447337.

1059 Kory, N., A.R. Thiam, R.V. Farese Jr, and T.C. Walther. 2015. Protein Crowding Is a Determinant of
1060 Lipid Droplet Protein Composition. *Dev Cell*. 34:351–363. doi:10.1016/j.devcel.2015.06.007

1061 Krahmer, N., Y. Guo, F. Wilfling, M. Hilger, S. Lingrell, K. Heger, H.W. Newman, M. Schmidt-
1062 Supprian, D.E. Vance, M. Mann, R.V.F. Jr, and T.C. Walther. 2011. Phosphatidylcholine
1063 Synthesis for Lipid Droplet Expansion Is Mediated by Localized Activation of
1064 CTP:Phosphocholine Cytidylyltransferase. *Cell Metab*. 14:504–515.
1065 doi:10.1016/j.cmet.2011.07.013.

1066 Lord, S.J., K.B. Velle, R.D. Mullins, and L.K. Fritz-Laylin. 2020. SuperPlots: Communicating
1067 reproducibility and variability in cell biology. *J Cell Biol*. 219:94–10. doi:10.1083/jcb.202001064.

1068 Lundquist, P.K., K.-K. Shivaiah, and R. Espinoza-Corral. 2020. Lipid droplets throughout the
1069 evolutionary tree. *Prog Lipid Res*. 78:101029. doi:10.1016/j.plipres.2020.101029.

1070 McClements, D.J., and C.E. Gumus. 2016. Natural emulsifiers — Biosurfactants, phospholipids,
1071 biopolymers, and colloidal particles: Molecular and physicochemical basis of functional
1072 performance. *Adv Colloid Interface Sci*. 234:3–26. doi:10.1016/j.cis.2016.03.002.

1073 McManaman, J.L., W. Zabaronick, J. Schaack, and D.J. Orlicky. 2003. Lipid droplet targeting
1074 domains of adipophilin. *J Lipid Res*. 44:668–673. doi:10.1194/jlr.C200021-JLR200.

1075 Mejhert, N., L. Kuruvilla, K.R. Gabriel, S.D. Elliott, M.-A. Guie, H. Wang, Z.W. Lai, E.A. Lane, R.
1076 Christiano, N.N. Danial, R.V. Farese Jr, and T.C. Walther. 2020. Partitioning of MLX-Family
1077 Transcription Factors to Lipid Droplets Regulates Metabolic Gene Expression. *Mol Cell*.
1078 77:1251–1264.e9. doi:10.1016/j.molcel.2020.01.014.

1079 Melchior, J.T., R.G. Walker, A.L. Cooke, J. Morris, M. Castleberry, T.B. Thompson, M.K. Jones,
1080 H.D. Song, K.-A. Rye, M.N. Oda, M.G. Sorci-Thomas, M.J. Thomas, J.W. Heinecke, X. Mei, D.
1081 Atkinson, J.P. Segrest, S. Lund-Katz, M.C. Phillips, and W.S. Davidson. 2017. A consensus
1082 model of human apolipoprotein A-I in its monomeric and lipid-free state. *Nat Struct Mol Biol*.
1083 24:1093–1099. doi:10.1038/nsmb.3501.

1084 Mirheydari, M., S.S. Rathnayake, H. Frederick, T. Arhar, E.K. Mann, S. Cocklin, and E.E. Kooijman.
1085 2016. Insertion of perilipin 3 into a glycerol(phospho)lipid monolayer depends on lipid headgroup
1086 and acyl chain species. *J Lipid Res*. 57:1465–1476. doi:10.1194/jlr.M068205.

1087 Miura, S., J.-W. Gan, J. Brzostowski, M.J. Parisi, C.J. Schultz, C. Londos, B. Oliver, and A.R.
1088 Kimmel. 2002. Functional Conservation for Lipid Storage Droplet Association among Perilipin,
1089 ADRP, and TIP47 (PAT)-related Proteins in Mammals, Drosophila, and Dictyostelium. *J Biol*
1090 *Chem*. 277:32253–32257. doi:10.1074/jbc.M204410200.

1091 Nakamura, N., and T. Fujimoto. 2003. Adipose differentiation-related protein has two independent
1092 domains for targeting to lipid droplets. *Biochem Biophys Res Commun*. 306:333–338.
1093 doi:10.1016/S0006-291X(03)00979-3.

1094 Nakamura, N., T. Akashi, T. Taneda, H. Kogo, A. Kikuchi, and T. Fujimoto. 2004. ADRP is
1095 dissociated from lipid droplets by ARF1-dependent mechanism. *Biochem Biophys Res Commun*.
1096 322:957–965. doi:10.1016/j.bbrc.2004.08.010.

1097 Ohsaki, Y., M. Suzuki, and T. Fujimoto. 2014. Open Questions in Lipid Droplet Biology. *Chemistry*
1098 & *Biology*. 21:86–96. doi:10.1016/j.chembiol.2013.08.009.

1099 Olzmann, J.A., and P. Carvalho. 2019. Dynamics and functions of lipid droplets. *Nat Rev Mol Cell*
1100 *Biol.* 1–19. doi:10.1038/s41580-018-0085-z.

1101 Osterman, N., J. Derganc, and D. Svenšek. 2016. Formation of vortices in long microcavities at low
1102 Reynolds number. *Microfluidics and Nanofluidics*. 20:33.

1103 Pace, C.N., and J.M. Scholtz. 1998. A helix propensity scale based on experimental studies of peptides
1104 and proteins. *Biophys j.* 75:422–427.

1105 Pataki, C.I., J. Rodrigues, L. Zhang, J. Qian, B. Efron, T. Hastie, J.E. Elias, M. Levitt, and R.R.
1106 Kopito. 2018. Proteomic analysis of monolayer-integrated proteins on lipid droplets identifies
1107 amphipathic interfacial α -helical membrane anchors. *Proc Natl Acad Sci USA*. 115:E8172–E8180.
1108 doi:10.1073/pnas.1807981115.

1109 Phillips, M.C. 2013. New insights into the determination of HDL structure by apolipoproteins:
1110 Thematic Review Series: High Density Lipoprotein Structure, Function, and Metabolism. *J Lipid*
1111 *Res.* 54:2034–2048. doi:10.1194/jlr.R034025.

1112 Pourmousa, M., H.D. Song, Y. He, J.W. Heinecke, J.P. Segrest, and R.W. Pastor. 2018. Tertiary
1113 structure of apolipoprotein A-I in nascent high-density lipoproteins. *Proc Natl Acad Sci USA*.
1114 115:5163–5168. doi:10.1073/pnas.1721181115.

1115 Prévost, C., M.E. Sharp, N. Kory, Q. Lin, G.A. Voth, R.V. Farese, and T.C. Walther. 2018.
1116 Mechanism and Determinants of Amphipathic Helix-Containing Protein Targeting to Lipid
1117 Droplets. *Dev Cell*. 44:73–86.e4. doi:10.1016/j.devcel.2017.12.011.

1118 Rowe, E.R., M.L. Mimmack, A.D. Barbosa, A. Haider, I. Isaac, M.M. Ouburai, A.R. Thiam, S. Patel,
1119 V. Saudek, S. Siniossoglou, and D.B. Savage. 2016. Conserved Amphipathic Helices Mediate
1120 Lipid Droplet Targeting of Perilipins 1–3. *J Biol Chem*. 291:6664–6678.
1121 doi:10.1074/jbc.M115.691048.

1122 Pucadyil, T.J., and S.L. Schmid. 2010. Supported Bilayers with Excess Membrane Reservoir: A
1123 Template for Reconstituting Membrane Budding and Fission. *Biophys. J.* 99:517–525.
1124 doi:10.1016/j.bpj.2010.04.036.

1125 Ruggieri, A., S. Naumenko, M.A. Smith, E. Iannibelli, F. Blasevich, C. Bragato, S. Gibertini, K.
1126 Barton, M. Vorgerd, K. Marcus, P. Wang, L. Maggi, R. Mantegazza, J.J. Dowling, R.A. Kley, M.
1127 Mora, and B.A. Minassian. 2020. Multiomic elucidation of a coding 99-mer repeat-expansion
1128 skeletal muscle disease. *Acta Neuropathologica*. 1–5. doi:10.1007/s00401-020-02164-4.

1129 Saito, H., P. Dhanasekaran, D. Nguyen, P. Holvoet, S. Lund-Katz, and M.C. Phillips. 2003. Domain
1130 Structure and Lipid Interaction in Human Apolipoproteins A-I and E, a General Model. *J Biol*
1131 *Chem*. 278:23227–23232. doi:10.1074/jbc.M303365200.

1132 Saleem, M., S. Morlot, A. Hohendahl, J. Manzi, M. Lenz, and A. Roux. 2015. A balance between
1133 membrane elasticity and polymerization energy sets the shape of spherical clathrin coats. *Nat*
1134 *Commun*. 6:6249. doi:10.1038/ncomms7249.

1135 Santinho, A., V.T. Salo, A. Chorlay, S. Li, X. Zhou, M. Omrane, E. Ikonen, and A.R. Thiam. 2020.
1136 Membrane Curvature Catalyzes Lipid Droplet Assembly. *Curr Biol*. 1–21.
1137 doi:10.1016/j.cub.2020.04.066.

1138 Schagger, H., and G. von Jagow. 1987. Tricine-sodium dodecyl sulfate-polyacrylamide gel
1139 electrophoresis for the separation of proteins in the range from 1 to 100 kDa. *Anal Biochem.*
1140 166:368–379.

1141 Schekman, R., and L. Orci. 1996. Coat proteins and vesicle budding. *Science.* 271:1526–1533.

1142 Scherer, P.E., P.E. Bickel, M. Kotler, and H.F. Lodish. 1998. Cloning of cell-specific secreted and
1143 surface proteins by subtractive antibody screening. *Nat Biotechnol.* 16:581–586.
1144 doi:10.1038/nbt0698-581.

1145 Schindelin, J., I. Arganda-Carreras, E. Frise, V. Kaynig, M. Longair, T. Pietzsch, S. Preibisch, C.
1146 Rueden, S. Saalfeld, B. Schmid, J.-Y. Tinevez, D.J. White, V. Hartenstein, K. Eliceiri, P.
1147 Tomancak, and A. Cardona. 2012. Fiji: an open-source platform for biological-image analysis.
1148 *Nat Meth.* 9:676–682. doi:10.1038/nmeth.2019.

1149 Soni, K.G., G.A. Mardones, R. Sougrat, E. Smirnova, C.L. Jackson, and J.S. Bonifacino. 2009.
1150 Coatomer-dependent protein delivery to lipid droplets. *J Cell Sci.* 122:1834–1841.
1151 doi:10.1242/jcs.045849.

1152 Sorre, B., A. Callan-Jones, J. Manzi, B. Goud, J. Prost, P. Bassereau, and A. Roux. 2012. Nature of
1153 curvature coupling of amphiphysin with membranes depends on its bound density. *Proc Natl*
1154 *Acad Sci USA.* 109:173–178. doi:10.1073/pnas.1103594108.

1155 Stenkula, K.G., and C. Erlanson-Albertsson. 2018. Adipose cell size: importance in health and disease.
1156 *Am J Physiol Regul Integr Comp Physiol.* 315:R284–R295. doi:10.1152/ajpregu.00257.2017.

1157 Subramanian, V., A. Garcia, A. Sekowski, and D.L. Brasaemle. 2004. Hydrophobic sequences target
1158 and anchor perilipin A to lipid droplets. *J Lipid Res.* 45:1983–1991. doi:10.1194/jlr.M400291-
1159 JLR200.

1160 Sztalryd, C., and D.L. Brasaemle. 2017. The perilipin family of lipid droplet proteins: Gatekeepers of
1161 intracellular lipolysis. *BBA - Mol Cell Biol Lipids.* 1862:1221–1232.
1162 doi:10.1016/j.bbalip.2017.07.009.

1163 Targett-Adams, P., D. Chambers, S. Gledhill, R.G. Hope, J.F. Coy, A. Girod, and J. McLauchlan.
1164 2003. Live Cell Analysis and Targeting of the Lipid Droplet-binding Adipocyte Differentiation-
1165 related Protein. *J Biol Chem.* 278:15998–16007. doi:10.1074/jbc.M211289200.

1166 Taylor, M.J., D. Perrais, and C.J. Merrifield. 2011. A High Precision Survey of the Molecular
1167 Dynamics of Mammalian Clathrin-Mediated Endocytosis. *PLoS Biol.* 9:e1000604.
1168 doi:10.1371/journal.pbio.1000604.s013.

1169 Thiam, A.R., B. Antonny, J. Wang, J. Delacotte, F. Wilfling, T.C. Walther, R. Beck, J.E. Rothman,
1170 and F. Pincet. 2013a. COPI buds 60-nm lipid droplets from reconstituted water-phospholipid-
1171 triacylglyceride interfaces, suggesting a tension clamp function. *Proc Natl Acad Sci USA.*
1172 110:13244–13249. doi:10.1073/pnas.1307685110.

1173 Thiam, A.R., R.V. Farese Jr, and T.C. Walther. 2013b. The biophysics and cell biology of lipid
1174 droplets. *Nat Rev Mol Cell Biol.* 14:775–786. doi:10.1038/nrm3699.

1175 Vrhovec, S., M. Mally, B. Kavčič, and J. Derganc. 2011. A microfluidic diffusion chamber for
1176 reversible environmental changes around flaccid lipid vesicles. *Lab Chip.* 11:4200–4206.
1177 doi:10.1039/c1lc20531e.

1178 Wilfling, F., A.R. Thiam, M.-J. Olarte, J. Wang, R. Beck, T.J. Gould, E.S. Allgeyer, F. Pincet, J.
1179 Bewersdorf, R.V. Farese, and T.C. Walther. 2014. Arf1/COPI machinery acts directly on lipid

1180 droplets and enables their connection to the ER for protein targeting. *Elife*. 3:e01607.
1181 doi:10.7554/eLife.01607.

1182 Wilfling, F., H. Wang, J.T. Haas, N. Krahmer, T.J. Gould, A. Uchida, J.-X. Cheng, M. Graham, R.
1183 Christiano, F. Fröhlich, X. Liu, K.K. Buhman, R.A. Coleman, J. Bewersdorf, R.V. Farese, and
1184 T.C. Walther. 2013. Triacylglycerol synthesis enzymes mediate lipid droplet growth by
1185 relocalizing from the ER to lipid droplets. *Dev Cell*. 24:384–399.
1186 doi:10.1016/j.devcel.2013.01.013.

1187 Wolins, N.E., B.K. Quaynor, J.R. Skinner, A. Tzekov, M.A. Croce, M.C. Gropler, V. Varma, A. Yao-
1188 Borengasser, N. Rasouli, P.A. Kern, B.N. Finck, and P.E. Bickel. 2006. OXPAT/PAT-1 Is a
1189 PPAR-Induced Lipid Droplet Protein That Promotes Fatty Acid Utilization. *Diabetes*. 55:3418–
1190 3428. doi:10.2337/db06-0399.

1191 Wolins, N.E., B.K. Quaynor, J.R. Skinner, M.J. Schoenfish, A. Tzekov, and P.E. Bickel. 2005. S3-12,
1192 Adipophilin, and TIP47 package lipid in adipocytes. *J Biol Chem*. 280:19146–19155.
1193 doi:10.1074/jbc.M500978200.

1194 Wolins, N.E., J.R. Skinner, M.J. Schoenfish, A. Tzekov, K.G. Bensch, and P.E. Bickel. 2003.
1195 Adipocyte protein S3-12 coats nascent lipid droplets. *J Biol Chem*. 278:37713–37721.
1196 doi:10.1074/jbc.M304025200.

1197 Zechner, R., F. Madeo, and D. Kratky. 2017. Cytosolic lipolysis and lipophagy: two sides of the same
1198 coin. *Nat Rev Mol Cell Biol*. 18:671–684. doi:10.1038/nrm.2017.76.

1199 Zhang, T., J. Lei, H. Yang, K. Xu, R. Wang, and Z. Zhang. 2011. An improved method for whole
1200 protein extraction from yeast *Saccharomyces cerevisiae*. *Yeast*. 28:795–798.
1201 doi:10.1002/yea.1905.

1202 Zimmermann, L., A. Stephens, S.-Z. Nam, D. Rau, J. Kübler, M. Lozajic, F. Gabler, J. Söding, A.N.
1203 Lupas, and V. Alva. 2018. A Completely Reimplemented MPI Bioinformatics Toolkit with a New
1204 HHpred Server at its Core. *J Mol Biol*. 430:2237–2243. doi:10.1016/j.jmb.2017.12.007.

1205

1206

1207

Figure legends

Figure 1. Plin4 AH forms very stable oil particles. **A.** Helical wheel representations of Plin4 and Plin4 4T>S AHs. **B.** Summary of LD localization of Plin4 AH and mutants (Copic et al., 2018). **C.** A 10 µl drop of triolein was added to 190 µl of HK buffer containing the indicated proteins (Plin4 12mer, Plin4 4mer or 4T>S, all at 0.5 mg/ml). After vigorous vortexing, the samples were photographed. **D.** Dynamics of Plin4 12mer interaction with oil as assessed by FRAP assays. Emulsions of triolein with unlabelled Plin4 12mer (0.5 mg/ml) and Alexa488-labelled Plin4 12mer (0.025 mg/ml) 12mer were prepared as in C and visualized by fluorescence microscopy. FRAP was performed on large droplets, which were entirely bleached (top row), or in the bulk as a control (middle row). The lower row shows a FRAP experiment performed on a limited region of the droplet. A summary of all FRAP experiments is shown in Figure 1 – Figure supplement 1B. **E.** FRAP of Plin4 4mer (0.5 mg/ml) mixed with Alexa488-labelled Plin4 4mer (0.01 mg/ml). **F.** Light microscopy images of Plin4 12mer and 4T>S emulsions at different time points after preparation by vortexing. **G.** Size distribution as assessed by dynamic light scattering (DLS) of a Plin4 12mer/triolein emulsion from 3 hours to 28 days after the vortexing reaction. Experiment was repeated two times. Scale bars: 5 µm.

Figure 1 – Figure supplement 1. Summary of FRAP experiments on oil droplets. **A.** Examples of FRAP experiments on oil droplets formed with Plin4 4T>S mutant. Emulsions of triolein were prepared with a solution of 4T>S (0.5 mg/ml) and Alexa488-4T>S (0.025 mg/ml). FRAP was performed using the same protocol as for Plin4 12mer. Note that there were very few droplets present in this suspension. Scale bar: 5 µm. **B.** Summary of the results of all FRAP experiments on oil droplets formed with Plin4 12mer, Plin4 4mer or 4T>S (4mer) mutant.

Figure 2. Real-time monitoring of protein–oil interaction in a microfluidic system shows irreversible adsorption of Plin4 12mer-A488 on triolein. **A.** Scheme of the microfluidics experimental set-up. **B.** Top row: confocal images of the triolein-buffer interface as formed in the microfluidic system after adsorption of Alexa488-labelled Plin4 12mer on the triolein surface and after rinsing with buffer. Bottom row: control experiment with the free fluorophore Alexa488. The intensity profile along the channel center is shown below each confocal image. The protein adsorbs irreversibly at the oil surface, whereas Alexa488 conjugated to free cysteine (A488) does not. See also Videos 1-4. A representative of 3 independent experiments is shown. **C.** Time course of the signal of Alexa488-labelled Plin4 12mer or of free Alexa-488 in the side channel as quantified from the experiment shown in B. A representative of 3 independent experiments is shown.

Video 1: Adsorption of Plin4 onto the triolein interface.

A confocal time-lapse recording of diffusion of Alexa-488-labelled Plin4 12mer into the side microfluidic channel and its adsorption onto the triolein interface. The relative fluorescence intensity profile along the channel center is shown at the bottom. Scale bar: 100 µm.

Video 2: Plin4 remains bound onto the triolein interface after rinsing.

A confocal time-lapse recording of rinsing the side microfluidic channel with buffer after Alexa-488-labelled Plin4 12mer adsorbed to the triolein interface (see Video 1). The fluorescence intensity profile along the channel center is shown at the bottom. Scale bar: 100 μm .

Video 3: Alexa-488 dye does not adsorb onto the triolein interface.

A confocal time-lapse recording of Alexa-488 dye diffusion into the side microfluidic channel towards the triolein meniscus. The relative fluorescence intensity profile along the channel center is shown at the bottom. Scale bar: 100 μm .

Video 4: Rinsing completely removes Alexa-488.

A confocal time-lapse recording of rinsing Alexa-488 dye out of the side microfluidic channel. The fluorescence intensity profile along the channel center is shown at the bottom. Scale bar: 100 μm .

Figure 2 – Figure supplement 1. Microfluidic experiments demonstrate that Plin4 12mer lowers the surface tension of oil. **A.** Plin4 12mer readily adsorbed to both oil and glass surfaces and even intercalated into the oil-glass interface, making the glass surface visibly heterogeneous (Videos 1 and 2). In this way, it induced a marked hysteresis in the oil-glass contact angle. The range of equilibrium contact angles spanned from 69° to 75° for buffer, and from 58° to 84° for Plin4 12mer. This hysteresis can result from chemical heterogeneities on a flat glass substrate (Joanny and De Gennes, 1984). **B.** Equilibrium pressure difference vs curvature for buffer (black points) and Plin4 12mer (blue points). The slope of the lines represents the surface tension of the interface. In the case of oil-buffer interface the surface tension was $36 \pm 3 \text{ mN/m}$ ($N=5$), and for PLIN4-12mer, the surface tension decreased to $25 \pm 1 \text{ mN/m}$ ($N=5$).

Figure 2 – Figure supplement 2. Plin4 mutant 4T>S-A488 also adsorbs to the oil surface, but is outcompeted by Plin4 12mer-A488. **A.** Confocal images of the oil-buffer interface in the microfluidic system after adsorption of Plin4 4mer mutant 4T>S-A488 (0.1 mg/ml) on the oil surface and after rinsing with buffer. The intensity profile along the channel center is shown below each confocal image. **B.** Time evolution of signal intensity on the oil surface and in the bulk solution during adsorption and rinsing. A representative of 3 independent experiments is shown. **C.** Competition between Plin4 12mer and 4T>S mutant. The ratio between the intensity on the oil surface and in the bulk solution for a mixture of unlabelled Plin4 12mer : Plin4 12mer-A488 (50:1) and a mixture of unlabelled 4T>S : Plin4 12mer-A488 (50:1). Mean \pm SD of the fluorescence intensity of surface/bulk solution is shown.

Figure 3. Comparison of the LD binding properties of perilipin AHs in yeast. **A.** Helical wheel representation of the AHs of Plin1 (aa 110-189 aa), Plin2 (aa 101-191 aa), Plin3 (aa 114-204) and Plin4 (aa 246-377, corresponding to the Plin4 4mer construct). In the case of Plin1, Plin2 and Plin3, the predicted AH regions are interspersed by short aa linkers, which are also indicated. Diagrams above the helical wheels show the full-length proteins, with AH regions shown in orange and the 4-helix bundle in dark grey. **B.** AA composition of the AH of

Plin1, 2, 3 and 4 (in %) in comparison with the average aa composition of vertebrate proteins (av. vert). The blue and red backgrounds indicate lower or higher % as compared to vertebrate values, respectively. **C.** Localization of GFP fusions with the AH region of Plin1, Plin2, Plin3 or Plin4 in *S. cerevisiae* cells. The experiment was performed with wild-type yeast cells (upper row), with *pet10Δ* cells (medium row) grown for 24h to stationary phase, or with *pet10Δ* cells grown to stationary phase and then transferred for 24h to oleic acid (OA) medium (lower row). Scale bar: 5 μm. **D.** Bar plots of the percentage of cells showing intracellular puncta for the different proteins expressed. 60 cells per each condition were counted in one of at least two representative experiments. **E.** Quantification of the size distribution of fluorescent LDs (labelled with GFP-fusion proteins) in *pet10Δ* + OA cells. The plots show representative measurements from two independent experiments, where the following number of LDs was counted: Plin1 AH, 141; Plin2 AH, 143; Plin3 AH, 136; Plin4 6mer, 148; Plin4 12mer, 159. Pixel size: 0.091 μm x 0.091 μm.

Figure 3-source data 1. Comparison of the LD binding properties of perilipin AHs in yeast and their effect on LD size.

Figure 3 – Figure supplement 1. Plin AH fusion proteins co-localize with LDs in yeast and are expressed at similar levels. **A.** Co-localization of Plin1 AH, Plin2 AH, Plin3 AH and Plin4 12mer mCherry fusions and LDs, stained with Bodipy in *pet10Δ* cells grown in oleic acid. Scale bar: 5 μm. **B.** Western blot analysis of yeast protein lysates from *pet10Δ* cells expressing Plin AH-GFP fusions as indicated. Experiment was repeated 3 times using different extraction methods.

Figure 4. Dynamics of perilipin AH-GFP fusions on LDs or at the plasma membrane in yeast. **A.** Dynamics of AH-GFP fusions on LDs in *pet10Δ* cells grown for 48h in oleic acid. Images show two representative FRAP time-courses in cells expressing Plin3 AH-GFP (top panels) or Plin4 12mer-GFP (bottom panels); time (in seconds) is indicated on top. Cells are outlined in white and the bleached areas containing one LD are outlined in green. Graph shows recovery curves for Plin1 AH-GFP (n=29), Plin2 AH-GFP (n=14), Plin3 AH-GFP (n=16), or Plin4 12mer-GFP (n=24). **B.** Recovery curves for Plin1 AH-GFP (n=11) or Plin4 12mer-GFP (n=5) on LDs in *pet10Δ* cells in late exponential phase (small LDs). **C.** FRAP of Plin1 AH (n=14) and Plin4 12mer (n=15) at the PM in exponentially-growing *pet10Δ* cells. Images show two representative time-courses for Plin1 AH (top) and Plin4 12mer (bottom). Bleached areas are outlined in green. **D.** FRAP of Plin4 6mer-GFP (n=12), Plin4 8mer-GFP (n=7) and Plin4 12mer-GFP (n=7) at the PM in exponentially-growing wild-type cells. All graphs show the mean ± SD of the fluorescence recovery curves from n FRAP measurements on different LDs or different regions of the PM, as shown in the images. Scale bar: 5 μm.

Figure 4-source data 1. Dynamics of perilipin AH-GFP fusions on LDs or at the plasma membrane in yeast assessed by FRAP.

Figure 4 – Figure supplement 1. Cell-to-cell variability in the recovery of Plin4 12mer-GFP after photobleaching of LDs in Drosophila S2 cells. FRAP was performed on oleic acid-induced LDs in S2 cells stably transfected with Plin4 12mer-GFP. **A.** Fluorescence recovery curves from individual cells in the same experiment performed in control cells (RNAi against luciferase). Each curve represents mean \pm SD from FRAP on 3 LDs in the same cell, as exemplified in the two images below the graph, showing two cells before bleaching. Areas that were bleached are marked with green circles. Fast fluorescence recovery was observed in the cell on the left, slow in the cell on the right. The fluorescence signal in the two images was acquired under the same settings, showing that the total Plin4-GFP expression level in the two cells was similar. However, note the difference in the amount of cytosolic signal. Scale bar: 5 μ m. **B.** Same as A, except that FRAP was performed on cells in which CCT1 has been depleted by RNAi. **C.** Correlation between the ratio of LD/cytosolic Plin4 12mer-GFP signal and the half-time of recovery, as determined from the curves shown in A and B. Each dot represents one cell, data is from two independent experiments. Asterisks denote cells which had very slow recovery kinetics (half-time > 100 s; in this case the value was set to 100 s).

Figure 5. Plin3 AH interacts much less strongly with oil than Plin4 AH. **A.** Turbidity assays with 0.5 mg/ml protein solutions of Plin4 12 mer, Plin4 4mer, Plin4 4mer mutant [4T>S], or Plin3 AH after vigorous vortexing with triolein (15 μ l for 285 μ l of protein solution). **B.** Size distribution of the droplets in triolein emulsions formed with Plin4 4mer or Plin3 AH at various times after vortexing was determined by DLS. Particle size is shown by volume weighted distributions. One of 3 independent experiments is shown. **C.** Protein/oil emulsions or protein solutions of the indicated variants of Plin4 or Plin3 AH were mixed with sucrose and loaded on the bottom of a sucrose step gradient. After centrifugation, four fractions were collected from the bottom and equal volumes were analysed by protein gels with Sypro Orange staining. **D.** Quantification (mean \pm SD) of the experiment in C. The number of repeats for each experiment is indicated above the bar graphs. **E.** Protein exchange assay in LD emulsions. Top panel: a Plin4 12mer (0.5 mg/ml) / triolein emulsion was prepared by vortexing. Thereafter, 0.025 mg/ml Alexa-488-labelled Plin4-12 mer was gently added. The emulsion was imaged at the indicated time points by light microscopy in bright field (BF) to see all particles and by fluorescence to detect coverage by Alexa-488-labelled Plin4 12 mer. Finally, the suspension was vortexed again to promote maximum incorporation of Alexa488-labelled Plin4 12mer in the emulsion. The middle and lower rows show similar experiments performed with Plin4 4mer and Plin3 AH emulsions, respectively. Scale bars: 5 μ m. **F.** Quantification (mean \pm SD) of the experiments shown in E as determined from four separate fields (73 x 100 μ m) in the same experiment. The graphs are representative of at least two independent experiments. Time on the x-axis is plotted using logarithmic scale. Asterisks indicates clustering of particles, which resulted a in low total number of fluorescent puncta, as seen in the image.

Figure 5-source data 1. Analysis of protein content and protein exchange in oil emulsions.

Figure 5 – Figure supplement 1. Plin3 AH purification and CD analysis. **A.** Tricine SDS-PAGE showing the purification of Plin3 AH after expression in *E. coli*. The lanes show the proteins present in the total bacteria extract (total) and after a 4-step protocol, which includes centrifugation to separate the soluble and the precipitated fractions, boiling and centrifugation of the soluble fraction to get the heat-resistant fraction, dialysis of the heat resistant fraction (boiled & dialyzed) and anion exchange chromatography with a gradient of NaCl from 10 to 1000 mM. Gel stained with SyproOrange. Molecular weight standards are indicated (in kDa). **B.** CD spectra showing ellipticity of Plin3 AH (25 μ M) in Tris buffer (blue line) or in buffer with 50% TFE (green line).

Figure 6. The polar face of Plin4 AH is key for specific and stable coating of LDs in cells. **A.** Weblogo plot of the AH region of human Plin4 as determined by aligning its 29 33-mer repeats. The vertical arrows indicate the mutated aa: the NQ pair (grey), which was mutated into NN, QQ or QN; the three K (blue), which were mutated into R, and the two D (red), which were mutated into E. **B.** Co-localization of GFP-Plin4 4mer wild-type and 3K>R (in white) with LDs (purple) in HeLa cells. **C.** Quantification of the percentage of LDs stained with the indicated protein per cell. These “SuperPlots” (Lord et al., 2020) show all data from 3 to 4 independent experiments, each with a different color; each light dot represents one cell, whereas each triangle shows the mean from one experiment. The black bars show the mean \pm SE of 3 to 4 independent experiments. **D.** Helical wheels of Plin4 WT and csw mutant. **E.** Localization of Plin4 12mer wild-type or csw mutant in HeLa cells. The insets show extended views with the protein in purple and LDs in green (stained with Bodipy). The super plots show the mean \pm SE of the % of LDs positive for the indicated protein per HeLa cell as determined from 3 independent experiments. **F.** CD spectra of Plin4 12mer (5 μ M) and csw 12mer (7.5 μ M) in solution (blue) or in an equal volume of buffer and TFE (green). **G.** Light microscopy images of mCherry fusions of Plin4 12mer wild-type or csw mutant in yeast. Top: mCherry fluorescence (mCh); bottom co-localization of mCherry (purple) with LDs stained with bodipy (green). The relative fluorescence signal of mCherry fusions of Plin4 12mer wild-type or csw mutant on LDs and at the PM in *PET10-GFP* yeast strain was used to build the SuperPlots shown on the right. Data are from three independent experiments, with $n \geq 25$ for each condition in each assay. **G.** Fluorescence recovery curves of mCherry fusions of Plin4 4mer 2T>V (green points) and 2T>V csw mutants (blue points) on LDs in HeLa cells. Each curve represents FRAP of a single LD in one cell.

Figure 6-source data 1. The polar face of Plin4 AH is key for specific and stable coating of LDs in cells.

Figure 6 – Figure supplement 1. Plin4 4mer mutants are not affected in their helical folding. **A.** CD spectra showing mean residue ellipticity (MRE) of purified Plin4 4mer (19 μ M), 4T>S (19 μ M) and NN (6 μ M) mutants in Tris buffer (blue lines) or in buffer with 50% TFE (green lines). **B.** Tricine SDS-PAGE analysis of the relative concentrations of the purified proteins. Gel was stained with Coomassie Blue.

Figure 6 – Figure supplement 2. Additional data for Plin4 charge-swap mutant. **A.** SDS-PAGE analysis of purified Plin4 12mer and csw 12mer. Gel stained with Coomassie Blue. **B.** Western-blot analysis of Plin4 12mer-GFP and csw 12mer-GFP expression in WT yeasts, showing similar expression levels. Vps10 was used as loading control. **C.** Influence of redistribution of charge in Plin4 12mer on LD size in yeast. Plot shows distribution of LD size in *pet10Δ* cells incubated with OA for 24h and expressing GFP fusions of Plin4 12mer or csw 12mer mutant. Graph shows a representative of three independent experiments, with 270 LDs measured for each construct. Pixel size: 0.091 μm x 0.091 μm .

Figure 7. The distribution of charged residues in the polar face of Plin4 AH is key for stable coating of triolein *in vitro*. **A.** 15 μl triolein was added to 285 μl of HK buffer containing Plin4 12mer wild-type or the csw mutant (0.5 mg/ml each). After vigorous vortexing, the samples were photographed. **B.** DLS measurements of the hydrodynamic radius of particles in emulsions shown in (A), from two independent experiments (note that data in assay #1 for Plin4 12mer is the same as in Figure 1G at 3h). Dots represent peak maxima and vertical bars represent polydispersity from one representative measurement. **C.** A triolein emulsion was prepared with Plin4 12mer or csw 12mer mutant (0.5 mg/ml). At the indicated time, fluorescent Plin4 12mer-Alexa488 (0.025 mg/ml) was gently added. The emulsions were imaged in the bright field mode (BF) and by fluorescence to detect the incorporation of Plin4 12mer-Alexa488 into the proteolipid particles. Finally, the suspension was vortexed again to promote maximum incorporation of Plin4 12mer-Alexa488 in the emulsion. Scale bars: 5 μm . **D.** Quantification (mean \pm SD) of the experiment shown in B, as determined from four separate fields (73 x 100 μm) in the same experiment. The graphs are representative of at least two independent experiments. Time on the x-axis is plotted using logarithmic scale.

Figure 7-source data 1. Redistribution of charged residues of Plin4 AH affects particle size in oil emulsions and dynamics of protein-oil interaction.

Figure 8. Plin4 adopts a helical conformation at the surface of oil and forms a dense monolayer. **A.** CD analysis of three independent samples of Plin4 12mer-oil emulsion purified by sucrose step gradients (left panel), compared with CD spectra Plin4 12mer in a similar concentration range in Tris buffer (blue lines) or in buffer with 50% TFE (green lines) **B-D.** Measurement of Plin4 12mer density at the oil surface. (B) A mixture of Alexa488-labelled and unlabelled Plin4 12mer (1:20) was vortexed with oil and mean droplet surface fluorescence from two independent experiments was quantified. Each data point represents one droplet. (C) Fluorescent Plin4 12mer mixtures at the indicated ratio and concentration were incubated with bead-supported diphytanoyl bilayers. Scale bar: 5 μm . (D) Graph shows mean surface bead fluorescence from five experiments (A to F) with varying Plin4 12mer concentration, Alexa488- to unlabelled Plin4 ratio and number of beads ($1x = 1.7 \times 10^6 \pm 20\%$ in 30 μl), as indicated below the graph. Each data point represents one bead; lines indicate mean values for each experiment. Bottom row: Surface area of Plin4 12mer on oil was calculated in each experiment by dividing surface fluorescence on beads per Plin4 surface

density with surface fluorescence on oil (panel B); see Supplementary table 2 for details. **E.** Model of Plin4 AH binding to oil. 1: Plin4 AH is unfolded in solution and folds in contact with a hydrophobic surface. 2: Plin4 AH binds as a monomeric helix to the lipid surface, using its weakly-hydrophobic face. The interaction is stabilized by the length of the AH. Steps 1-2 are common for all perilipin AHs. 3: Plin4 AHs interact laterally via charged residues, forming a dense and highly stable coat-like lattice.

Figure 8-source data 1. Estimate of Plin4 12mer density on oil surface.

Tables

Table 1. Plasmids used in this study.

Name	Insert	Region (aa) (1)	Vector	Host (2)	Source
pCLG03	Plin4 4mer	hPlin4(246-377)	pET21b	E. coli	Copic 2018
pKE23	Plin4 12mer	hPlin4(510-905)	pET21b	E. coli	Copic 2018
pSB49	4T>S (4mer)	4x[246-278 M5t] (3)	pmCherry-N1	Mamm	Copic 2018
pMGA9	4T>S (4mer)	4x[246-278 M5t] (3)	pET21b	E. coli	This study
pGFP-Plin1	Human Plin1	Full cDNA	pGREG576 (ADH1pr, GFP)	Yeast	Jacquier 2013
pGFP-Plin2	Human Plin2	Full cDNA	pGREG576 (ADH1pr, GFP)	Yeast	Jacquier 2013
pGFP-Plin3	Human Plin3	Full cDNA	pGREG576 (ADH1pr, GFP)	Yeast	Jacquier 2013
pRHT140	ADHpr-mcs-GFP		pRS416 (CEN-URA3)	Yeast	S. Leon
pMGA4	ADHpr-mcs-mCherry (swap of GFP in pRHT140)		pRS416 (CEN-URA3)	Yeast	This study
pMGA11	Plin1 AH-GFP	hPlin1(aa108-194)	pRHT140	Yeast	This study
pMGA10	Plin1 AH-mChe	hPlin1(aa108-194)	pMGA4	Yeast	This study
pMGA6	Plin2 AH-GFP	hPlin2(aa100-192)	pRHT140	Yeast	This study
pMGA5	Plin2 AH-mCherry	hPlin2(aa100-192)	pMGA4	Yeast	This study
pMGA7	Plin3 AH-GFP	hPlin3(aa113-205)	pRHT140	Yeast	This study
pMGA29	Plin3(87-205)-GFP	hPlin3(aa87-205)	pRHT140	Yeast	This study
pMGA28	Plin3(87-205)-mCherry	hPlin3(aa87-205)	pMGA4	Yeast	This study
pMGA19	Plin3 AH	hPlin3(aa113 – 205)	pET21b	E. coli	This study
pKE31	Plin4 4mer-GFP	hPlin4(aa246-377)	pRHT140	Yeast	Copic 2018
pKE33	Plin4 12mer-GFP	hPlin4(aa510-905)	pRHT140	Yeast	Copic 2018
pMGA16	Plin4 12mer-mCherry	hPlin4(aa510-905)	pMGA4	Yeast	This study
pCLG26	Plin4 8mer	hPlin4(aa246-509)	pmCherry-N1	Mamm	Copic 2018

pMGA31	Plin4 6mer-GFP	hPlin4(aa246-433)	pRHT140	Yeast	This study
pMGA23	Plin4 8mer-GFP	hPlin4(aa246-509)	pRHT140	Yeast	This study
pACJ22	Plin4 4mer	hPlin4(aa246-377)	pmCherry-N1	Mamm	Copic 2018
pSB58	2D>E (4mer)	4x[246-278 M17e] (3)	pmCherry-N1	Mamm	This study
pSB60	NN (4mer)	4x[246-278 M18q] (3)	pmCherry-N1	Mamm	This study
pMGA32	NN (4mer)	4x[246-278 M18q] (3)	pET21b	E. coli	This study
pSB83	QN (4mer)	4x[246-278 M19qn] (3)	pmCherry-N1	Mamm	This study
pSB65	QQ (4mer)	4x[246-278 M20q2] (3)	pmCherry-N1	Mamm	This study
pSB86	3K>R	4x[246-278 M21r] (3)	pmCherry-N1	Mamm	This study
pCLG62	Plin4 12mer	hPlin4(aa510-905)	pmCherry-N1	Mamm	Copic 2018
pSB06	csw 12mer	Charge swap of hPlin4(aa510-905)	pmCherry-N1	Mamm	This study
pCLG36	Plin4 2T>V 4mer	4x[246-278 M10t2] (3)	pmCherry-N1	Mamm	Copic 2018
pACJ41	Plin4 csw 2T>V 4mer	Charge swap and 2T>V of 4x[246-278 M7kt] (3)	pmCherry-N1	Mamm	Copic 2018
pSB41	Plin4 12mer- GFP	hPlin4(aa510-905)	pMTWG	Dros.	Copic 2018
pMGA3	csw 12mer	Charge swap of hPlin4(aa510-905)- GFP	pRHT140	Yeast	This study
pMGA17	csw 12mer	Charge swap of hPlin4(aa510-905)- mCherry	pMGA4	Yeast	This study
pMGA1	csw 12mer	Charge swap of hPlin4(aa510-905)	pET21b	E. coli	This study

- (1) Position of amino acids (aa) in human perilipin sequences.
(2) Mamm: mammalian cells, Dros.: Drosophila cells
(3) All mutants are 4 repeats of the same amino acid sequence.

Supplementary files

Supplementary File 1. Summary of synthetic gene sequences and protein sequences used in this study.

Supplemental Table 2. Calculation of Plin4 12mer density on oil, related to Figure 8 B-D. Table summarizes input values and calculations for 5 experimental conditions (A-E) used to standardize the fluorescence of Alexa488 labelled Plin4 12mer on lipid surface, using bead-supported diphytanoyl bilayers as standards.

Experiment	A	B	C	D	E
Reaction volume (V)	30 μ l	30 μ l	30 μ l	30 μ l	30 μ l
[Plin4 12mer] (nM) ⁽¹⁾	80 (0.25)	80 (0.25)	80 (0.25)	80 (0.25)	32 (0.25)
Plin4*:Plin4 ratio (r) ⁽²⁾	1 : 20	1 : 5	1 : 5	1 : 5	1 : 5
Bead Number (N) ⁽³⁾	1.7 x 10 ⁶ (0.2)	1.7 x 10 ⁶ (0.2)	3.4 x 10 ⁶ (0.2)	5.1 x 10 ⁶ (0.2)	1.7 x 10 ⁶ (0.2)
Fraction of Plin4 bound to beads (f) ⁽⁴⁾	0.6 (0.17)	0.6 (0.17)	0.75 (0.13)	n.d.	0.6 (0.33)
Fl. Intensity on beads (A.U.) ($F_{Plin4\ bead}$) ⁽⁵⁾	225 (0.1)	1100 (0.23)	350 (0.21)	200 (0.5)	500 (0.15)
Fl. Intensity on oil ($F_{Plin4\ oil}$) ⁽⁶⁾	2350 (0.4)	2350 (0.4)	2350 (0.4)	2350 (0.4)	2350 (0.4)
Surface density of Plin4 12mer (nm ⁻²) ⁽⁷⁾	0.067 (0.55)	0.054 (0.59)	0.108 (0.57)	n.d.	0.048 (0.73)
Molecular area of Plin4 12mer (nm ²)	15 +/- 8	18.5 +/- 11	9.3 +/- 5.3	n.d.	21 +/- 15

(1) Concentration of Plin4 12mer was determined from SDS PAGE stained with Coomassie blue or SyprOrange after centrifugation at 100 000 g of thawed protein stock. Values are mean +/- relative SD (in parentheses) from 3 independent measurements.

(2) Unlabelled Plin4 12mer (Plin4) was mixed with Alexa488-labelled Plin4 12mer (Plin4*) at indicated molar ratios.

(3) Bilayer-supported beads were prepared as described, diluted in a 30x stock solution and counted under the microscope before adding it to the final reaction. The number of beads in the final reaction was determined from the concentration in stock solution and the dilution factor.

Total bead surface area was calculated by multiplying the number of beads in the reaction with surface area of an individual bead ($r = 5 \times 10^3$ nm).

(4) Fraction of Plin4 12mer bound to beads was determined in a fluorimeter by measuring the fluorescence of protein solution before and after incubation with beads for 15 min at RT. Values are mean +/- relative SD (in parentheses) from 3 independent measurements for each condition; n.d., not determined.

(5) Fluorescence intensity of Plin4 12mer-A488 on the surface of beads from the experiment shown in Fig. 8D. Values are mean +/- relative SD (in parentheses) from 20 beads per condition.

(6) Fluorescence intensity of Plin4 12mer-A488 on the surface of oil was determined in two independent experiments shown in Fig. 8B from 75 particles in total.

(7) Surface area density of Plin4 12mer on oil was calculated using the formula:

$$Surface\ Density = N_{av}[Plin4\ 12\ mer] \times f_{bound} \times \frac{1}{r} \times \frac{Vol_{reaction}}{(N_{beads} \times bead\ area)} \times \frac{F_{Plin4\ oil}}{F_{Plin4\ beads}}$$

where N_{av} is the Avogadro Number

Relative error given in parenthesis was calculated from the square root of the sum of all input relative error.

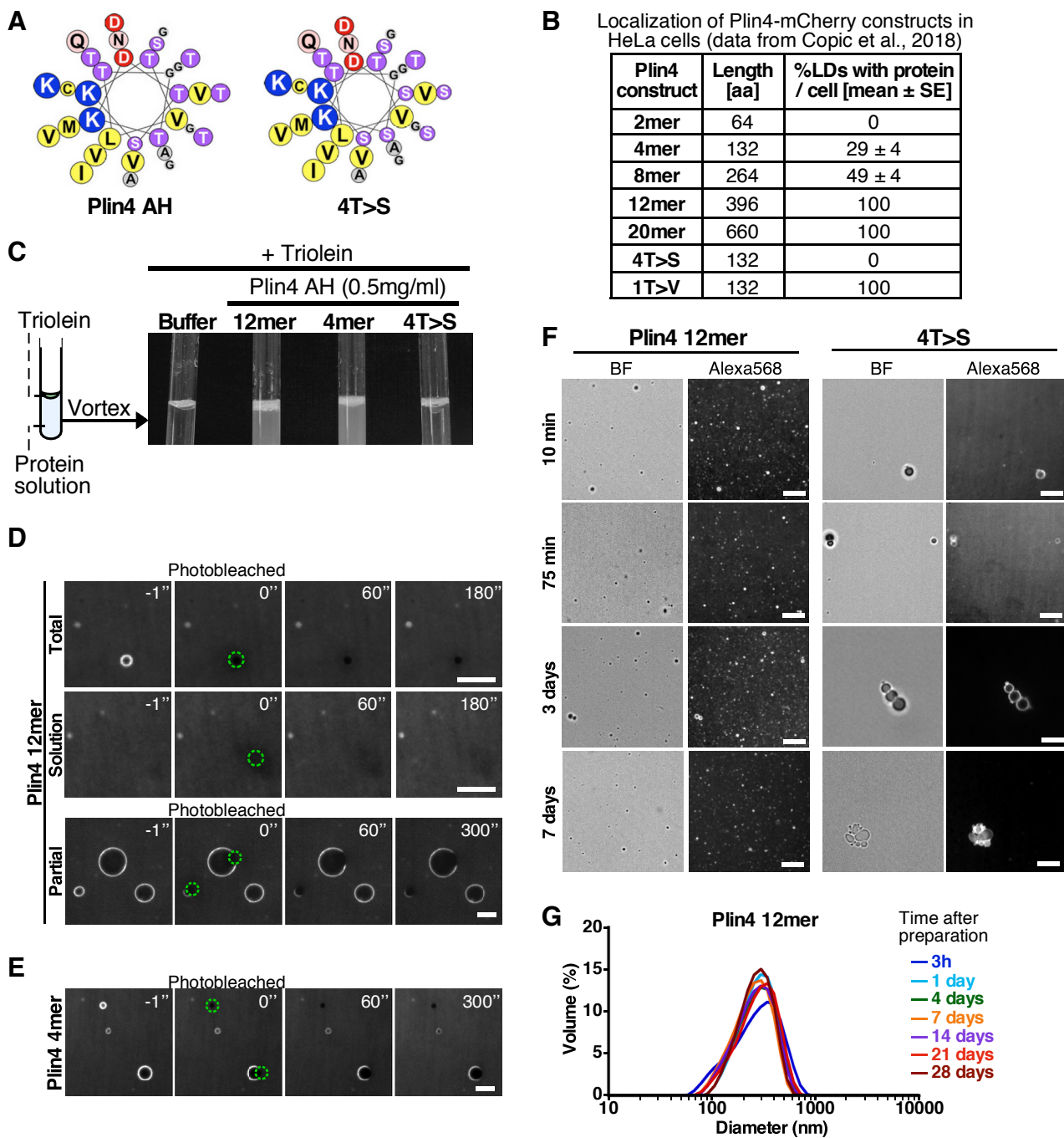
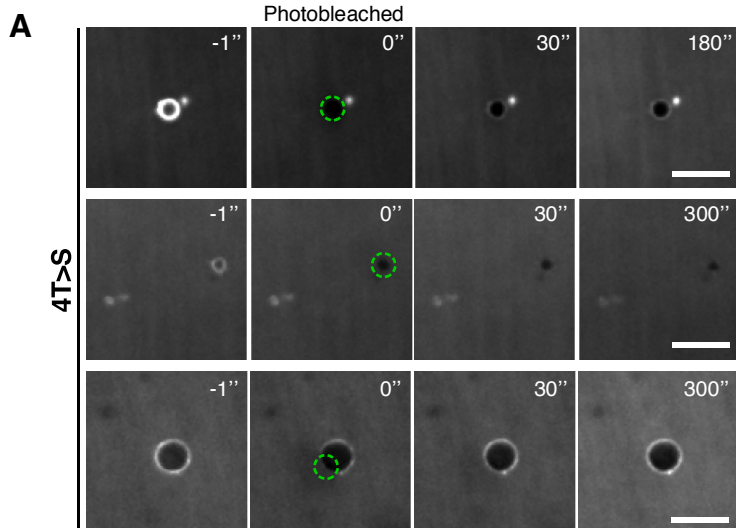
Figure 1

Figure 1 - Supplement 1



B

Protein	# Total FRAPs	# Recovery: Total FRAP	# Partial FRAPs	# Recovery: Partial FRAP
Plin4 12mer	15	0	6	0
Plin4 4mer	13	0	8	0
4T>S	8	2	5	4

Figure 3

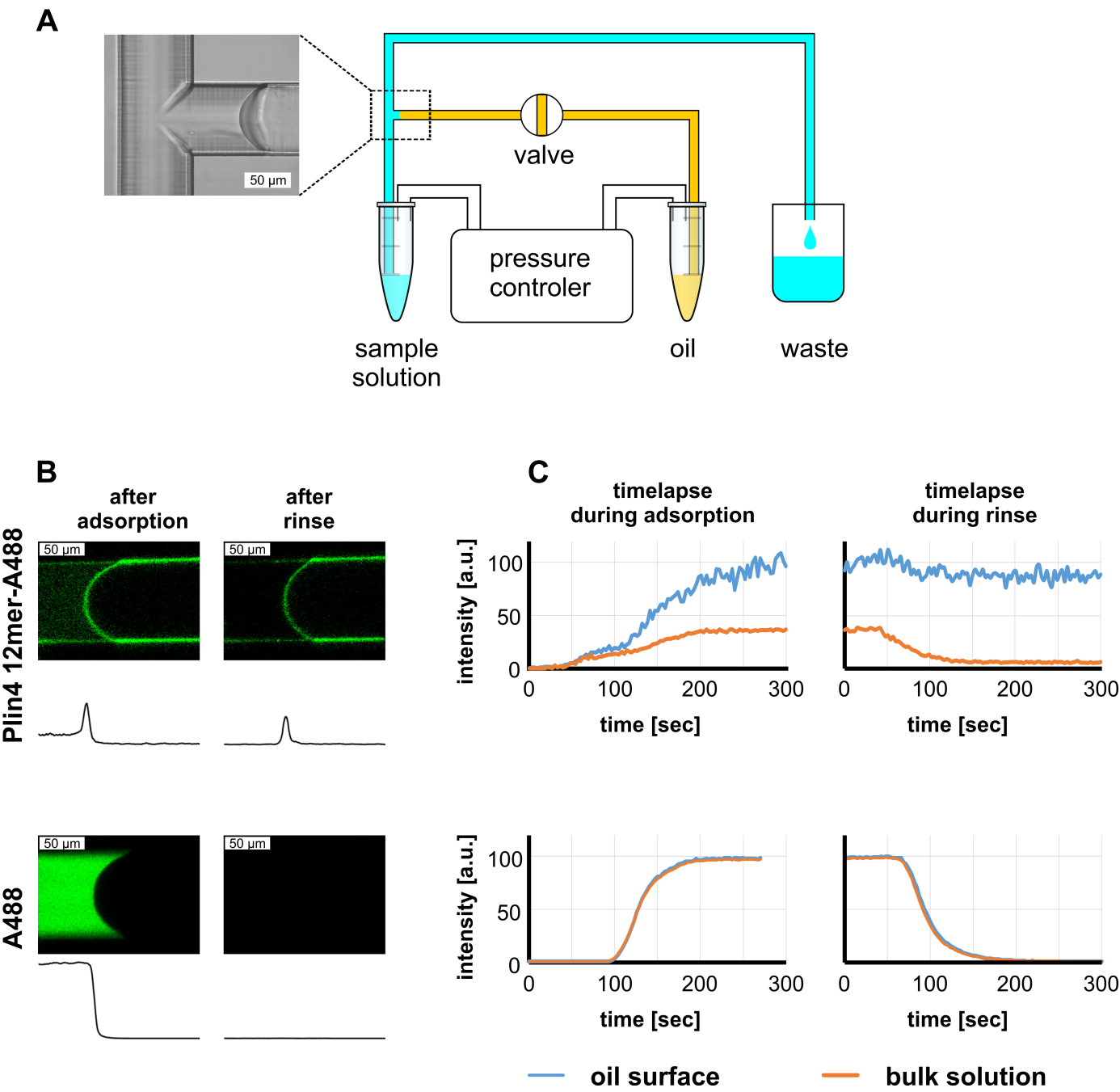
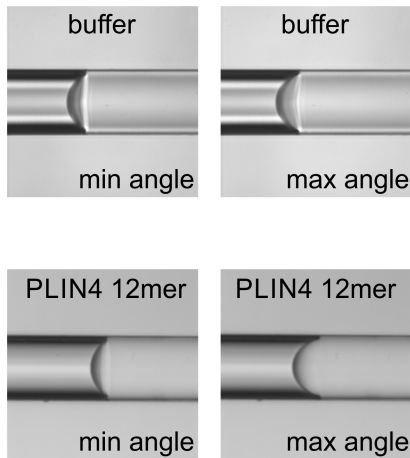


Figure 2 - figure supplement 1

A



B

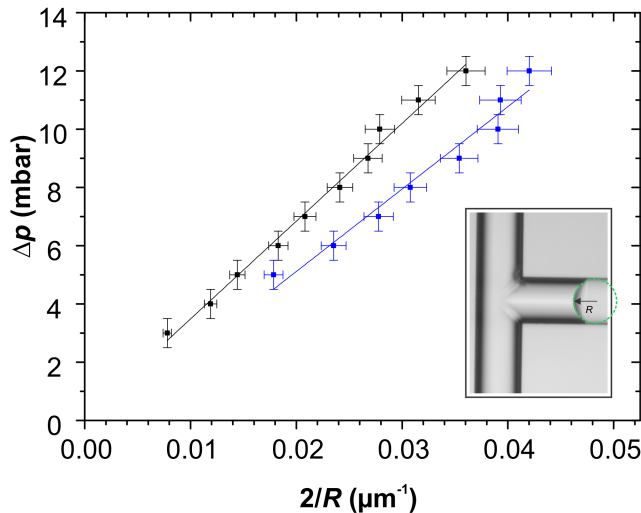
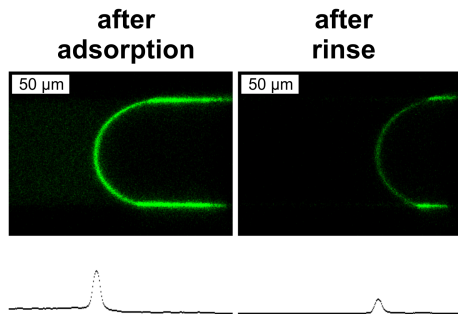


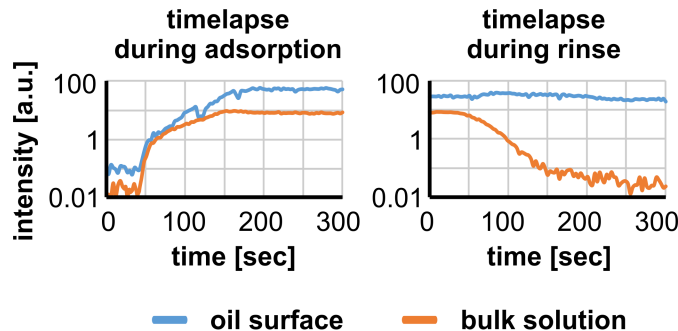
Figure 2 - figure supplement 2

Plin4 4T-S-A488

A

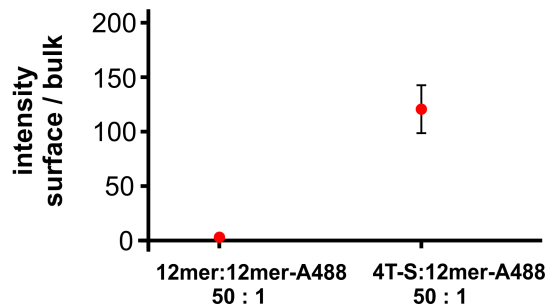
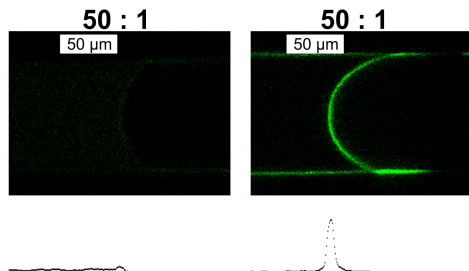


B



C

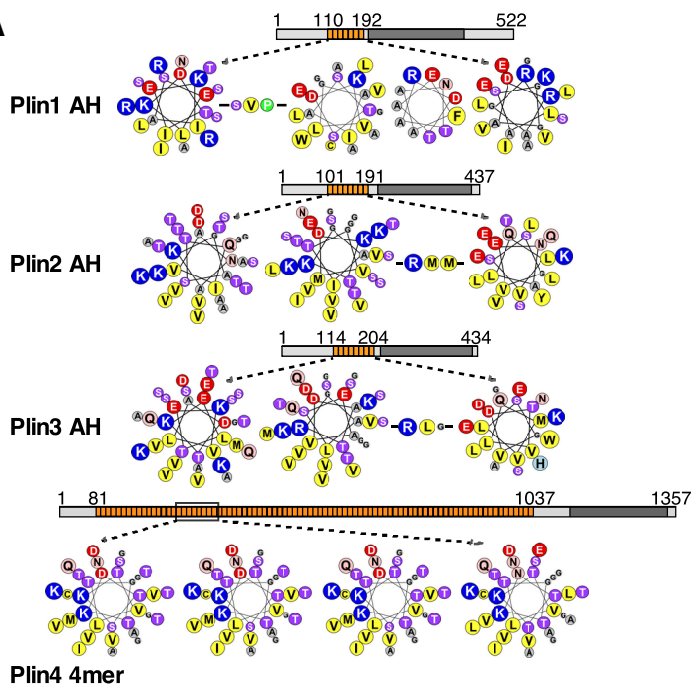
12mer:12mer-A488 4T-S:12mer-A488



Plin4

Figure 3

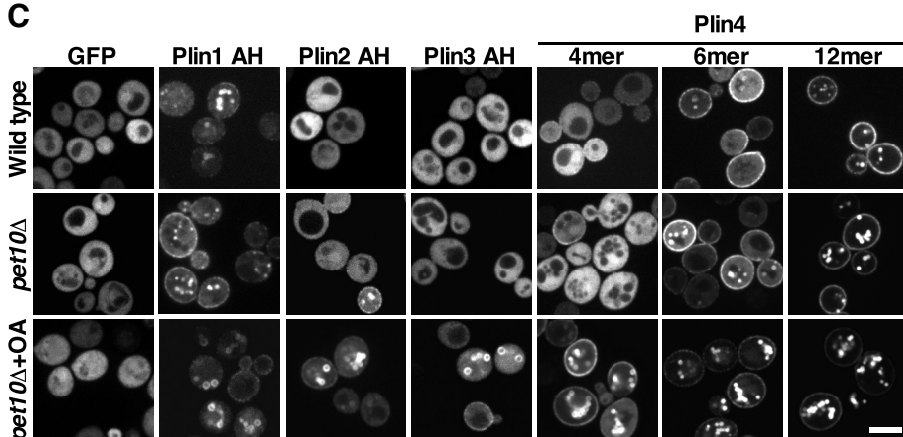
A



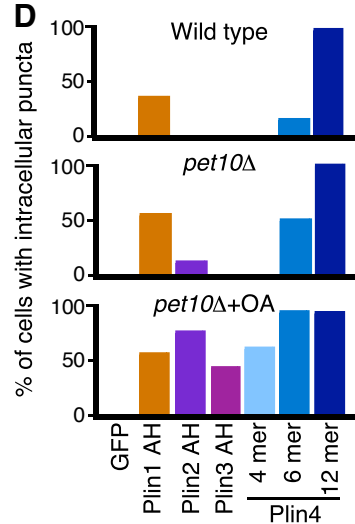
B

aa	Plin1	Plin2	Plin3	Plin4	Plin5	Av. vert
Trp + Phe	2.4	0	1.1	0.2	3.6	5.3
Leu + Ile	18.1	9.9	7.7	6.7	8.9	11.4
Val	6	15.4	16.5	15.0	23.3	6.8
Gly	8.4	9.9	9.9	15.6	3.6	7.4
Ala	18.1	9.9	8.8	10.8	7.1	7.4
Thr	6	14.3	8.8	21.3	5.4	6.2
Ser	10.8	12.1	13.2	5.4	14.3	8.1
Asn + Gln	2.4	6.6	6.6	6.5	0	10.2
Lys	4.8	8.8	7.7	8.8	5.4	7.2
Arg	7.2	1.1	2.2	0.4	8.9	4.2
Glu	7.2	4.4	6.6	0.3	8.9	3.7
Asp	4.8	3.3	6.6	5.3	7.1	5.9
AH length (aa)	83	91	91	957	56	

C



D



E

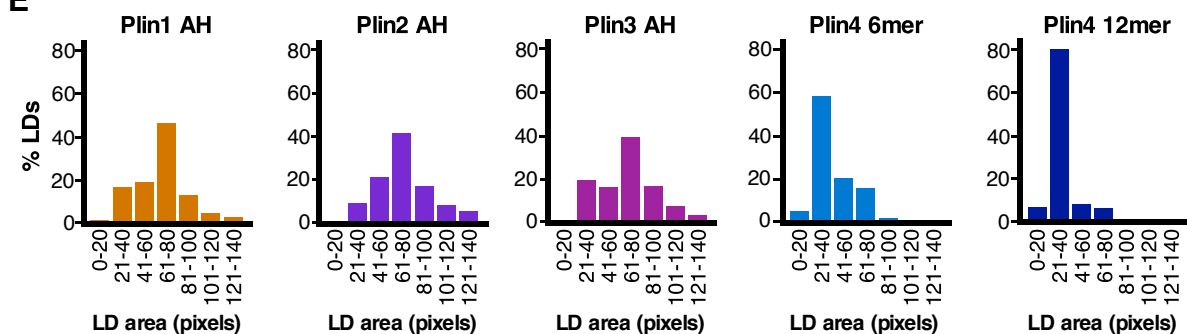
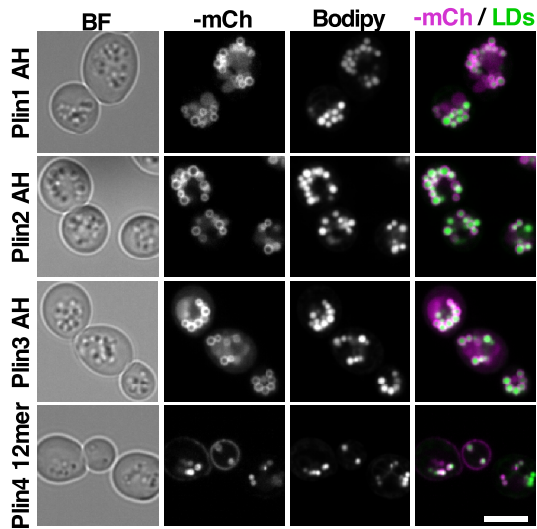


Figure 3 - Supplement 1

A



B

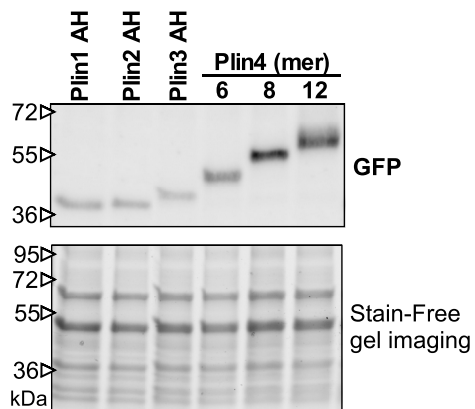


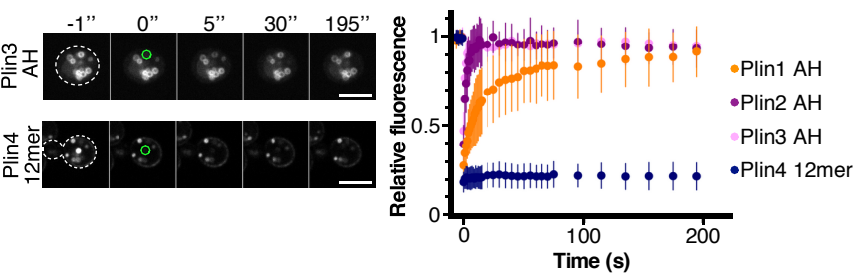
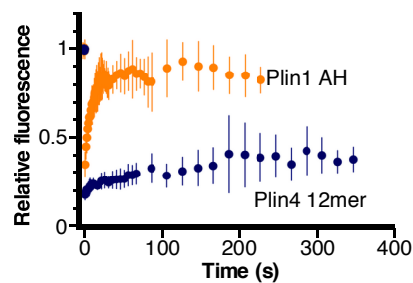
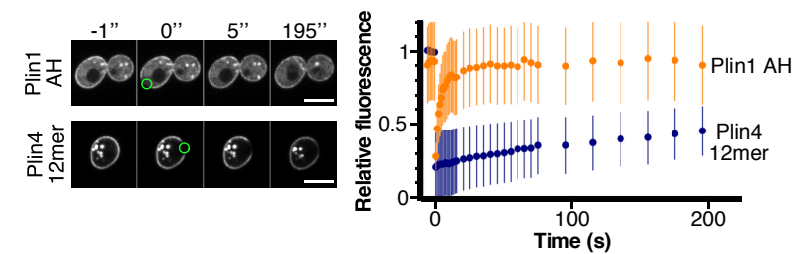
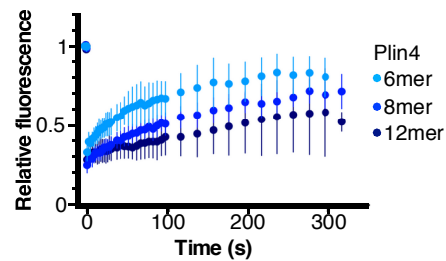
Figure 4**A****B****C****D**

Figure 4 - Supplement 1

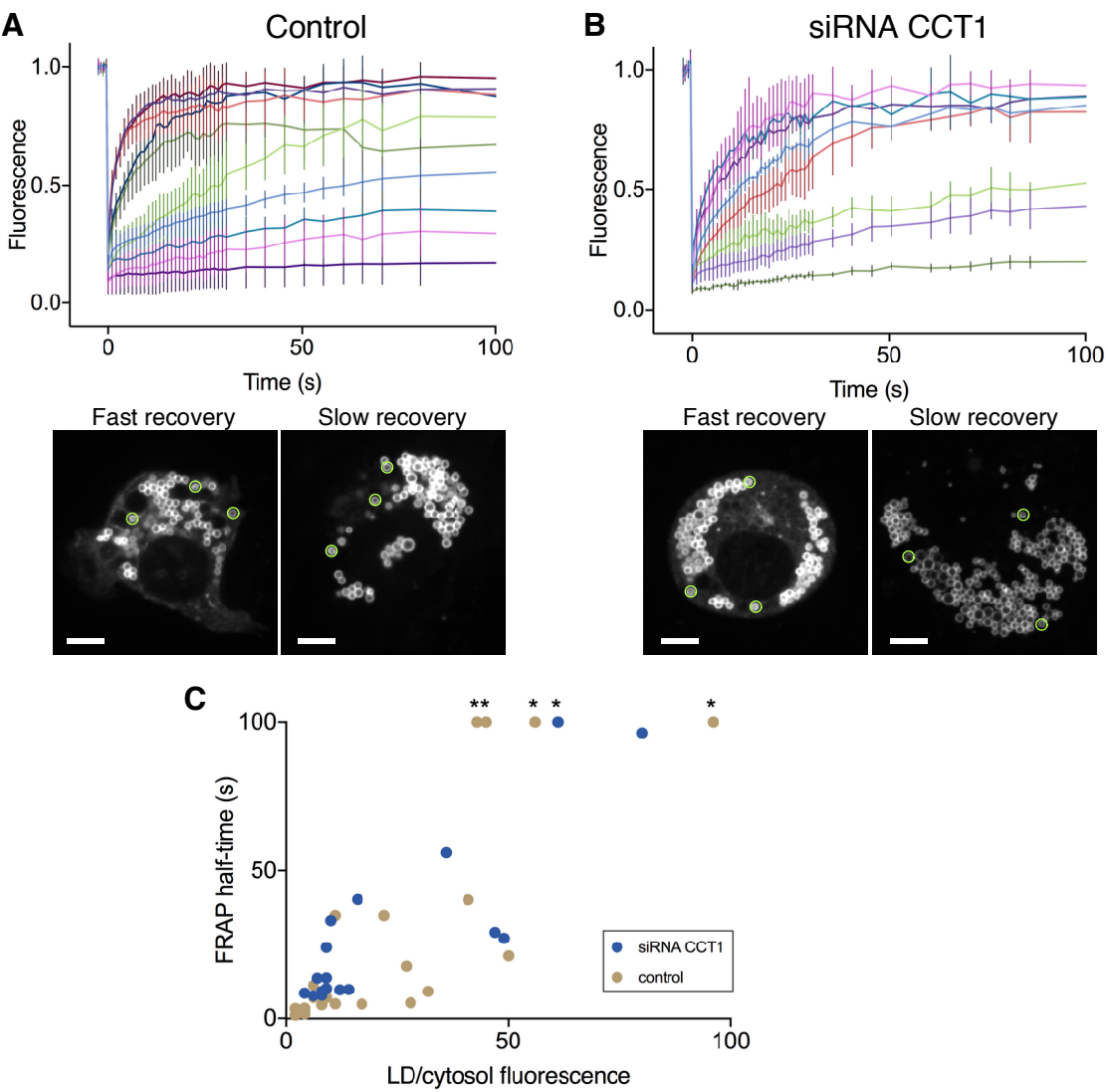


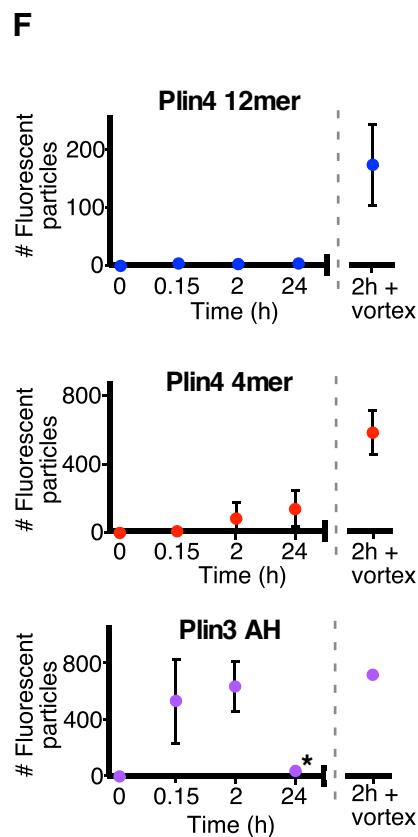
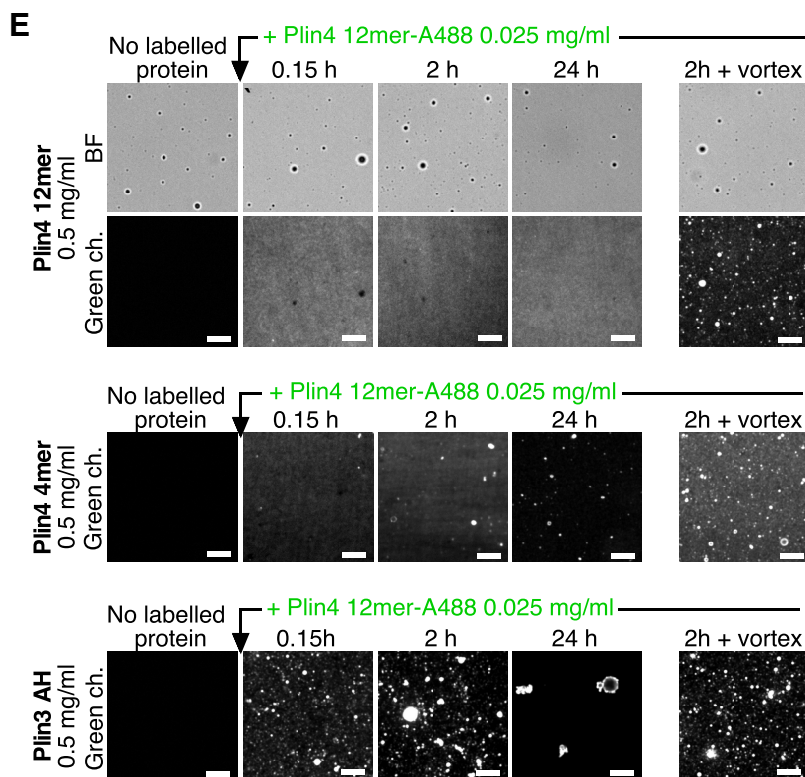
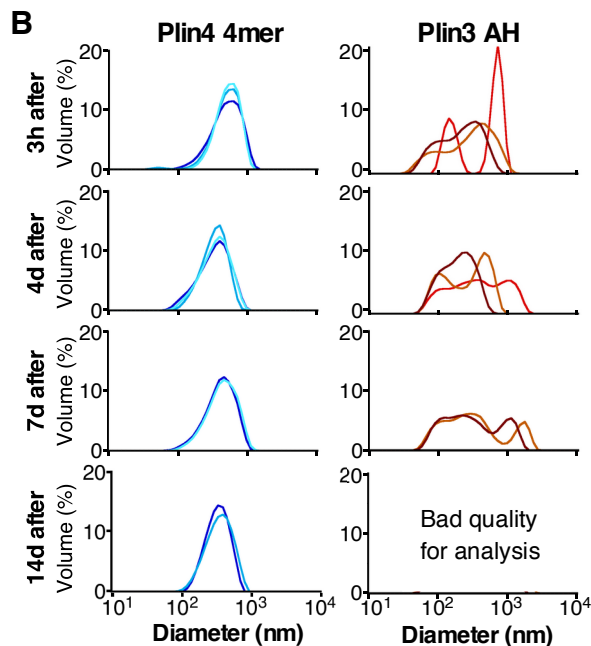
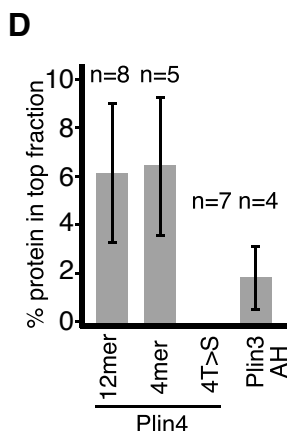
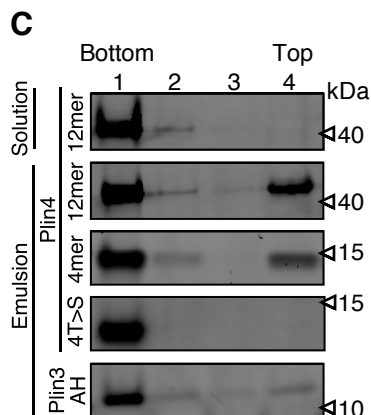
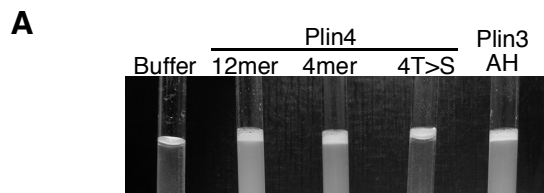
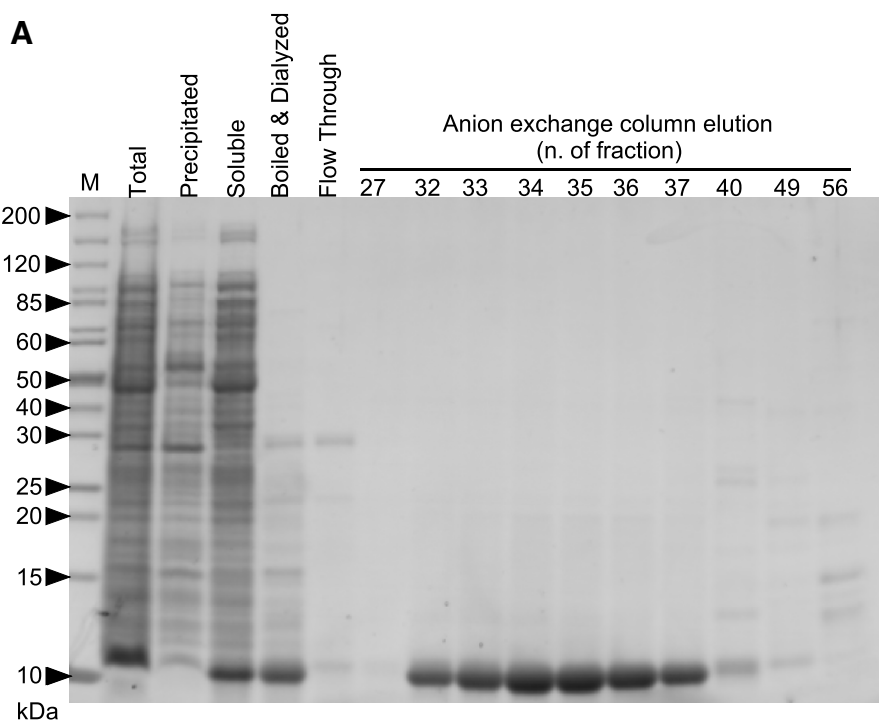
Figure 5

Figure 5 - Supplement 1

A



B

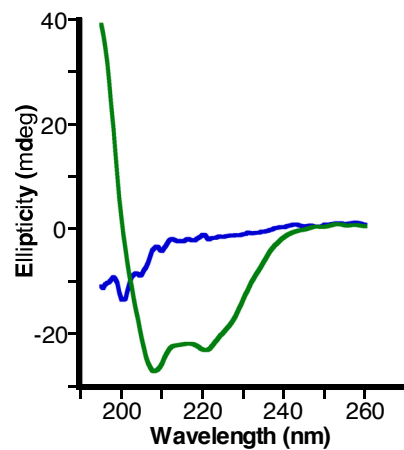


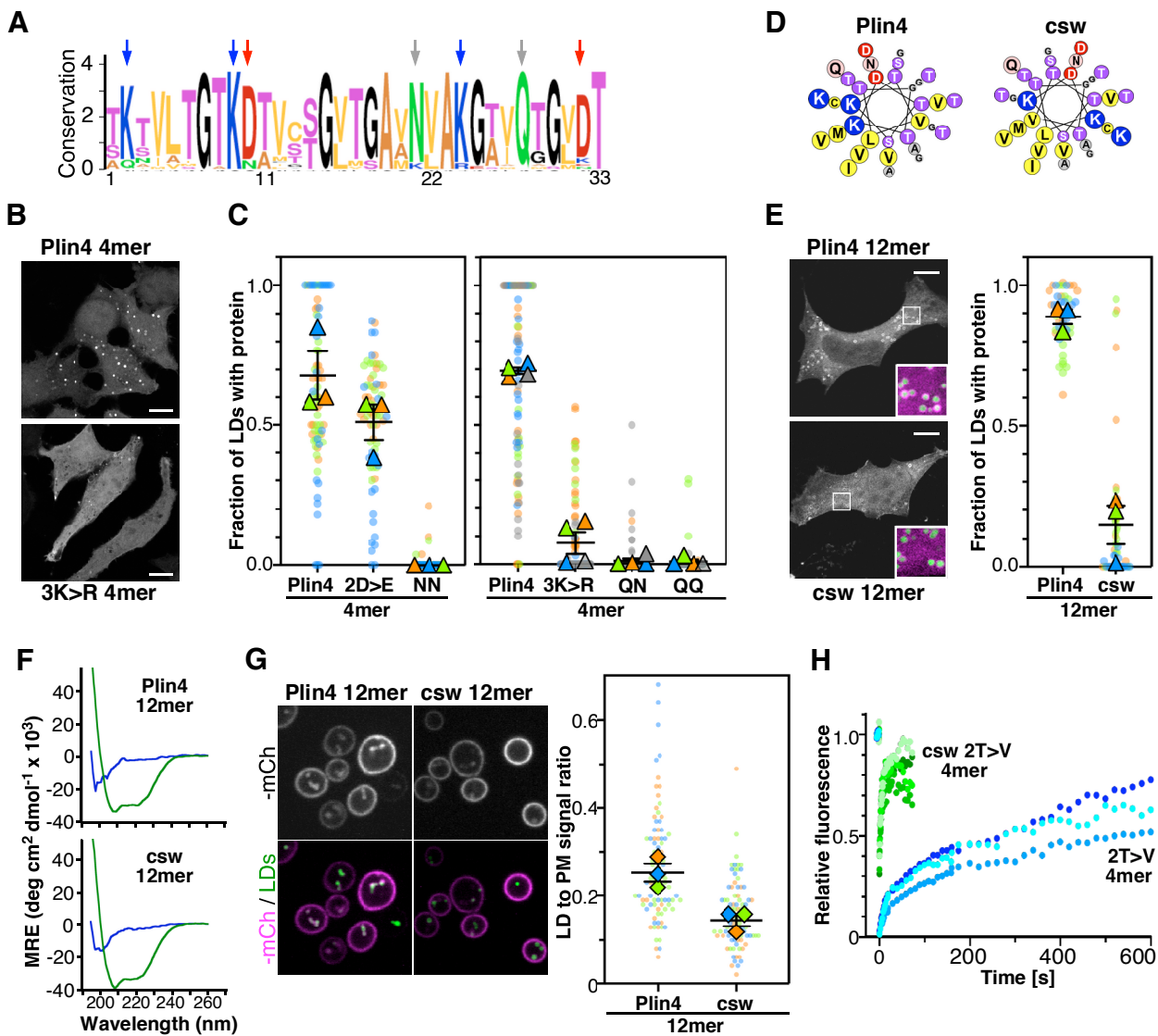
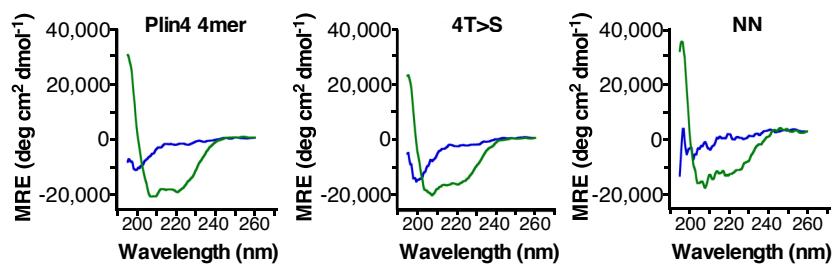
Figure 6

Figure 6 - Supplement 1

A



B

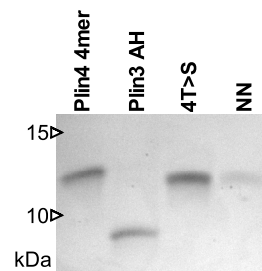


Figure 6 - Supplement 2

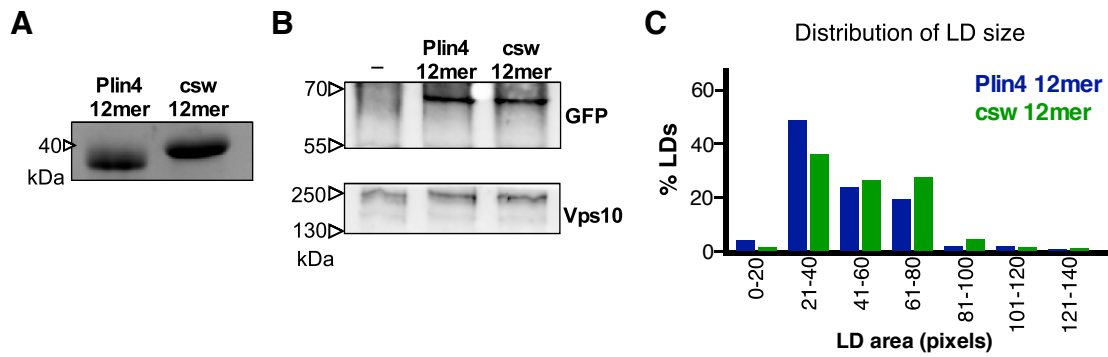


Figure 7

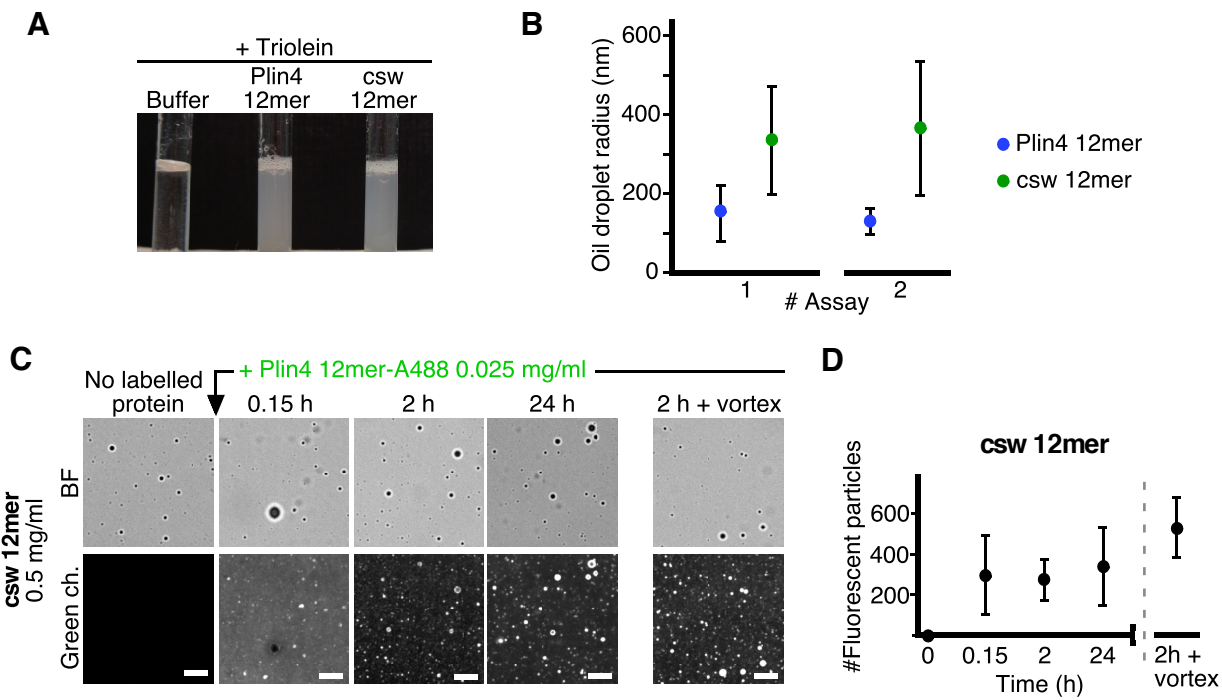


Figure 8

